

Multi-step phase transitions and gravitational waves in the inert doublet model

Nico Benincasa^{*a}, Luigi Delle Rose^{†b}, Kristjan Kannike^{‡a} and Luca Marzola^{§a}

^aNational Institute of Chemical Physics and Biophysics, Rävala 10, Tallinn, Estonia

^bDipartimento di Fisica, Università della Calabria, I-87036 Arcavacata di Rende, Cosenza, Italy

Dated: May 16, 2022

Abstract: The inert doublet model is a well-motivated extension of the Standard Model that contains a dark matter candidate and modifies the dynamics of the electroweak symmetry breaking. In order to detail its phenomenology, we perform a comprehensive study of cosmic phase transitions and gravitational wave signals implied by the framework, accounting for the latest results of collider experiments. We require the neutral inert scalar to constitute, at least, a subdominant part of the observed dark matter abundance. While most of the phase transitions proceed through a single step, we identify regions of the parameter space where the electroweak vacuum is reached after multiple phase transitions. The resulting gravitational wave spectrum is generally dominated by single-step transitions and, in part of the parameter space, falls within the reach of near-future gravitational wave detectors such as LISA or BBO. We find that direct detection experiments efficiently probe the part of parameter space associated with multi-step phase transitions, which remain unconstrained only in the Higgs resonance region testable with future monojet searches. The implications of the new determination of the W boson mass are also discussed.

1. Introduction

Although the discovery of the Higgs boson at the LHC [1, 2] brought to completion the search for Standard Model (SM) particles, we are far from having a complete description of Nature. The cosmological observations of the last thirty years, for instance, have revealed that the SM constituents explain only a small share of the total energy budget of the Universe. In particular, the analysis of the microwave radiation background shows that baryons constitute only about 15% of all matter [3]. The remaining part is accounted for by dark matter (DM), a substance of unknown nature which finds no description in the SM. Presently, the leading direct detection experiments have not yet found clear signals of DM scattering on nucleons or electrons, resulting in upper bounds on the direct detection cross sections [4–6]. Similarly, this far collider searches have not found any presence of DM particles in the produced states [7].

Problems arise also within the known boundaries of the SM, where the measured properties of the Higgs boson seem to indicate the metastability of the electroweak (EW) vacuum. Furthermore, the apparent absence of new degrees of freedom at the EW scale questions the known mechanisms deemed responsible for the stabilization of the Higgs boson mass scale, which seemingly remains insensitive to the large radiative contributions expected within most of the ultraviolet completions of the theory.

This lack of signals gives encouragement to look for other avenues in the attempt to pinpoint the possible physics beyond the SM. In regard of this, one important possibility is provided by the recent discovery of gravitational waves (GW) by the LIGO experiment [8, 9], which has opened a new window on the dynamics taking place in the early stages of the Universe. Crucially, GW astronomy allows us to explore cosmological phase transitions related to the dynamics of EW symmetry breaking. Given the measured properties of the Higgs boson, the EW phase transition (PT) predicted by the SM is a smooth cross-over [10, 11] which does not generate observable GW signals. However, scalar extensions of the SM can easily admit first-order phase transitions (FOPT) resulting in a stochastic GW background [12–14] within the reach of future space-based GW observatories such as LISA [15, 16],

^{*}nico.benincasa@kbfi.ee; corresponding author

[†]luigi.dellerose@unical.it

[‡]kristjan.kannike@cern.ch

[§]luca.marzola@cern.ch

BBO [17, 18], Taiji [19, 20], TianQuin [21] or DECIGO [22, 23]. Because the LHC discovery confirmed the existence of scalar fields in Nature, it is worth to consider possible applications of such models within particle physics and cosmology.

Following this line of reasoning, in the present paper we revisit the phenomenology of the Inert Doublet Model (IDM) [24–27], paying special attention to the reach of future GW experiments. The IDM is characterised by the presence of a second scalar doublet stabilised by a \mathbb{Z}_2 symmetry which – crucially – is *not* spontaneously broken. Consequently, the new field is ‘inert’: it cannot couple to the SM fermions via Yukawa interactions and it is forbidden from acquiring a non-vanishing vacuum expectation value (VEV) at zero temperature.

In spite of these restrictions, the IDM can give rise to a rich phenomenology. For instance, owing to the unbroken \mathbb{Z}_2 symmetry, the lightest neutral component of the new doublet is necessarily stable and, therefore, constitutes a viable DM candidate. In regard of this, previous studies have shown that the IDM can account fully for the observed DM relic density in two regions of its parameter space. One possibility is provided by the Higgs resonance region, where the mass of DM is close to half of the Higgs boson mass. Alternatively, in the large-mass region, the new scalar components have a compressed mass spectrum [28–30].

The DM and collider phenomenology of the IDM are well studied (see e.g. Refs. [31, 32] for a recent review). The phase diagrams of the IDM and the dependence of phase structure on the values of scalar quartic couplings were elucidated in Ref. [33]. While in the literature there are studies of the EW phase transitions within the IDM [34–37], we find that a full assessment, including a consistent treatment of bubble nucleation and the implied GW signal, is still missing. The possibility of realizing multi-step phase transitions, in particular, is intriguing because these processes can generate the multi-peak GW spectra considered first in Ref. [38]. This fascinating signature has been studied within the context of other two-Higgs-doublet models [37, 39–41], where the restrictions of the IDM are lifted. Within the IDM, instead, the cross-correlation between DM and phase transition phenomenology was investigated in Ref. [42].

With the present paper, we intend to improve on existing analyses pertaining to cosmic phase transitions within the IDM. To this purpose, we analyze the parameter space allowed by the latest collider and DM searches in the attempt to map the available phase transition patterns, as well as the GW signals they produce. Although most commonly the EW phase transitions occur in a single step ($O \rightarrow h$), we find regions of the parameter space where two-step ($O \rightarrow H \rightarrow h$ or $O \rightarrow hH \rightarrow h$) and even three-step ($O \rightarrow H \rightarrow hH \rightarrow h$) transitions are realised. We pay particular attention to two- and three-step processes that involve multiple first-order phase transitions, which have the potential to generate a clear GW signature presenting multiple peaks in the spectrum. In our analysis we impose that the DM relic density produced by the IDM does not exceed the 3σ upper bound indicated by the latest Planck measurement [3]. We also assess the impact of direct detection experiments, finding that they significantly constrain the parameter space yielding multi-step phase transitions with the exception of the Higgs resonance region. The latter will be completely probed in future monojet searches, which are therefore crucial to rule in or out the identified multi-step solutions.

In light of the new CDF determination of the W boson mass [43], we also present a separate analysis of the impact of the new measurement. In agreement with previous results [44], we observe that adopting the CDF value strongly reduces the number of viable DM solutions for DM masses of order $\mathcal{O}(100)$ GeV or larger, especially for phase transition patterns involving at least one first-order transition.

The paper is organised as follows. In Sec. 2, after presenting the IDM framework, we summarise the results concerning the quantum and thermal corrections received by the scalar potential. In Sec. 3, instead, we define the parameter space probed by our analysis and detail the theoretical and experimental constraints that we apply. Sec. 4 discusses the evolution of the vacuum and the patterns of cosmic phase transition that we have identified. The results obtained are then scrutinized in Sec. 5, where we analyze the impact of direct detection experiment and the power of future collider searches. The predicted GW signals are given in Sec. 6, whereas the implications of the new W boson mass are detailed in Sec. 7. Finally, we conclude by summarising our findings in Sec. 8.

2. The inert doublet model

2.1. Tree-level potential

The SM Higgs doublet H_1 and the inert doublet H_2 can be decomposed as

$$H_1 = \begin{pmatrix} G^+ \\ \frac{v+h+iG^0}{\sqrt{2}} \end{pmatrix}, \quad H_2 = \begin{pmatrix} H^+ \\ \frac{H+iA}{\sqrt{2}} \end{pmatrix}, \quad (1)$$

where h is the SM Higgs boson, $\langle h \rangle = v = 246.22$ GeV is the EW VEV and G^+ and G^0 are Goldstone bosons. The inert doublet comprises a charged scalar field H^\pm , and two neutral scalars, H and A , with opposite CP-parities.

The tree-level potential of the model,

$$V = -m_1^2 |H_1|^2 - m_2^2 |H_2|^2 + \lambda_1 |H_1|^4 + \lambda_2 |H_2|^4 + \lambda_3 |H_1|^2 |H_2|^2 + \lambda_4 |H_1^\dagger H_2|^2 + \frac{\lambda_5}{2} [(H_1^\dagger H_2)^2 + \text{h.c.}], \quad (2)$$

respects a discrete \mathbb{Z}_2 symmetry under which H_2 is odd and all the SM fields are even. The symmetry thus ensures the stability of the lightest component of the inert doublet and forbids new Yukawa couplings between H_2 and the SM fermions, hence the epithet *inert*.

The requirement that the tree-level potential be minimised at the EW vacuum leads to the following parametrization

$$\begin{aligned} m_1^2 &= \frac{m_h^2}{2}, & m_2^2 &= -m_H^2 + \lambda_{345} \frac{v^2}{2}, & \lambda_1 &= \frac{m_h^2}{2v^2}, & \lambda_3 &= \lambda_{345} + 2 \frac{m_{H^\pm}^2 - m_H^2}{v^2}, \\ \lambda_4 &= \frac{m_H^2 + m_A^2 - 2m_{H^\pm}^2}{v^2}, & \lambda_5 &= \frac{m_H^2 - m_A^2}{v^2}, \end{aligned} \quad (3)$$

given in terms of the tree-level scalar mass matrix eigenvalues m_h^2, m_H^2, m_A^2 and $m_{H^\pm}^2$ ($m_{G^0} = m_{G^\pm} = 0$ at tree-level in the EW vacuum).

The inert doublet self-coupling λ_2 does not affect DM phenomenology, but can influence the phase structure of the potential by inducing new minima at non-zero temperature. With the parametrization in Eq. (3), the model is completely specified by the quantities $\lambda_2, \lambda_{345} = \lambda_3 + \lambda_4 + \lambda_5$, and the masses m_H, m_{H^\pm}, m_A , which we use as input parameters in our analysis. The lightest neutral components of H_2 is a viable DM candidate. In our analysis, this role is assigned to H , in effect choosing $\lambda_5 < 0$. Equivalently, A could be the DM candidate, related to our case through the substitutions $\lambda_{345} \leftrightarrow \tilde{\lambda}_{345} = \lambda_3 + \lambda_4 - \lambda_5$ and $m_H \leftrightarrow m_A$.¹

For the treatment of the phase transitions in Section 4, we suppose that excursions in the field space occur only in the (h, H) plane, while the remaining scalar degrees of freedom are prevented from acquiring a VEV at any temperature. Therefore, the terms in the tree-level potential relevant for this analysis are

$$V_0(h, H) = -\frac{m_1^2}{2} h^2 + \frac{\lambda_1}{4} h^4 - \frac{m_2^2}{2} H^2 + \frac{\lambda_2}{4} H^4 + \frac{\lambda_{345}}{4} h^2 H^2. \quad (4)$$

2.2. Coleman-Weinberg correction to the potential

The tree-level potential in Eq. (2) receives important radiative contributions sourced by the one-loop n -point functions, re-summed in the Coleman-Weinberg correction [45]

$$V_{\text{CW}}(h, H) = \frac{1}{64\pi^2} \sum_i n_i m_i^4 \left(\ln \frac{m_i^2}{\mu^2} - C_i \right), \quad (5)$$

where $i = W, Z, t, h, H, G^0, A, G^\pm, H^\pm$ (as customary, we retain only the dominant fermion contribution given by the top quark), μ is the renormalization scale (which we set to $\mu = v$) and C_i are constants peculiar to

¹In regard of this, notice that $\lambda_5 \rightarrow -\lambda_5$ under the substitution $m_H \leftrightarrow m_A$ and that the quartic couplings determining the DM abundance via hHH or hAA interactions are, respectively, by λ_{345} and $\tilde{\lambda}_{345}$.

the renormalization scheme. The bosonic and fermionic contributions are weighted by the coefficients n_i given by $n_W = 6$, $n_Z = 3$, $n_t = -12$, $n_h = n_H = n_{G^0} = n_A = 1$ and $n_{H^\pm} = n_{G^\pm} = 2$ [46]. After using dimensional regularization with the $\overline{\text{MS}}$ subtraction scheme, we have $C_i = \frac{3}{2}$ for scalars, fermions and longitudinal vector bosons, as well as $C_i = \frac{1}{2}$ for transverse vector bosons. The field-dependent masses m_i^2 in Eq. (5) include, respectively, the eigenvalues of the neutral and charged scalar mass matrices

$$M_{S_1}^2 = \begin{pmatrix} -m_1^2 + 3\lambda_1 h^2 + \frac{\lambda_{345}}{2} H^2 & \lambda_{345} h H \\ \lambda_{345} h H & -m_2^2 + 3\lambda_2 H^2 + \frac{\lambda_{345}}{2} h^2 \end{pmatrix}, \quad (6)$$

$$M_{S_2}^2 = \begin{pmatrix} -m_1^2 + \lambda_1 h^2 + \frac{\tilde{\lambda}_{345}}{2} H^2 & \lambda_5 h H \\ \lambda_5 h H & -m_2^2 + \lambda_2 H^2 + \frac{\tilde{\lambda}_{345}}{2} h^2 \end{pmatrix}, \quad (7)$$

$$M_{\pm}^2 = \begin{pmatrix} -m_1 + \lambda_1 h^2 + \frac{\lambda_3}{2} H^2 & \frac{\lambda_4 + \lambda_5}{2} h H \\ \frac{\lambda_4 + \lambda_5}{2} h H & -m_2 + \lambda_2 H^2 + \frac{\lambda_3}{2} h^2 \end{pmatrix}, \quad (8)$$

as well as the EW gauge bosons and top-quark contributions

$$m_W^2 = \frac{1}{4} g_2^2 (h^2 + H^2), \quad m_Z^2 = \frac{1}{4} (g_1^2 + g_2^2) (h^2 + H^2), \quad m_t^2 = \frac{1}{2} y_t^2 h^2, \quad (9)$$

with g_1 , g_2 and y_t the $U(1)_Y$, $SU(2)_L$ and top-quark Yukawa couplings respectively.

Following previous analyses [37, 47, 48], we compensate possible radiative shifts of the EW VEV and address the problematic Goldstone contributions with a set of counterterms specified in

$$V_{\text{CT}}(h, H) = \delta m_h^2 h^2 + \delta m_H^2 H^2 + \delta \lambda_1 h^4, \quad (10)$$

where the coefficients are determined by the renormalization conditions

$$\left. \frac{\partial V_{\text{CT}}}{\partial h} \right|_{\text{VEV}} = - \left. \frac{\partial V_{\text{CW}}}{\partial h} \right|_{\text{VEV}}, \quad (11)$$

$$\left. \frac{\partial^2 V_{\text{CT}}}{\partial h^2} \right|_{\text{VEV}} = - \left(\left. \frac{\partial^2 V_{\text{CW}}}{\partial h^2} \right|_{G^0, G^\pm \equiv 0} + \frac{1}{32\pi^2} \sum_{G=G^0, G^\pm} \left(\frac{\partial m_G^2}{\partial h} \right)^2 \ln \left(\frac{m_{\text{IR}}^2}{\mu^2} \right) \right) \Big|_{\text{VEV}}, \quad (12)$$

$$\left. \frac{\partial^2 V_{\text{CT}}}{\partial H^2} \right|_{\text{VEV}} = - \left(\left. \frac{\partial^2 V_{\text{CW}}}{\partial H^2} \right|_{G^0, G^\pm \equiv 0} + \frac{1}{32\pi^2} \sum_{G=G^0, G^\pm} \left(\frac{\partial m_G^2}{\partial H} \right)^2 \ln \left(\frac{m_{\text{IR}}^2}{\mu^2} \right) \right) \Big|_{\text{VEV}}, \quad (13)$$

where VEV here corresponds to the zero-temperature vacuum $(h, H) = (v, 0)$ and m_{IR} is the infrared cutoff used for the regularization of Goldstone contributions, which we set to the Higgs boson mass, $m_{\text{IR}} = m_h$ [48].

2.3. Finite temperature effects

At finite temperature, thermal corrections result in a further contribution [49],

$$V_T(h, H, T) = \frac{T^4}{2\pi} \left[\sum_i n_i^{\text{B}} J_{\text{B}} \left(\frac{m_i^2}{T^2} \right) + \sum_i n_i^{\text{F}} J_{\text{F}} \left(\frac{m_i^2}{T^2} \right) \right], \quad (14)$$

to the scalar potential. The two sums are over the boson and fermion degrees of freedom, respectively and the corresponding thermal functions [50] are

$$J_{\text{B/F}}(x) = \int_0^\infty dt \, t^2 \ln \left(1 \mp e^{-\sqrt{t^2+x}} \right). \quad (15)$$

A consistent treatment of thermal corrections also requires the resummation of the leading self-energy daisy diagrams, which shifts the field-dependent masses

$$m_1^2(T) = m_1^2 - c_1 T^2, \quad m_2^2(T) = m_2^2 - c_2 T^2, \quad (16)$$

by a thermal contribution quantified in the coefficients [51, 52]

$$c_1 = \frac{1}{16}(g_1^2 + 3g_2^2) + \frac{1}{4}y_t^2 + \frac{6\lambda_1 + 2\lambda_3 + \lambda_4}{12}, \quad (17)$$

$$c_2 = \frac{1}{16}(g_1^2 + 3g_2^2) + \frac{6\lambda_2 + 2\lambda_3 + \lambda_4}{12}. \quad (18)$$

Thermal corrections also result in Debye masses for the longitudinal components of gauge bosons [53], given by

$$m_{W_L}^2 = \frac{h^2 + H^2}{4} g_2^2 + 2g_2^2 T^2, \quad (19)$$

$$m_{Z_L}^2 = \frac{h^2 + H^2}{8} (g_1^2 + g_2^2) + (g_1^2 + g_2^2) T^2 + \Delta, \quad (20)$$

$$m_{\gamma_L}^2 = \frac{h^2 + H^2}{8} (g_1^2 + g_2^2) + (g_1^2 + g_2^2) T^2 - \Delta, \quad (21)$$

with

$$\Delta^2 = \frac{(h^2 + H^2 + 8T^2)^2}{64} (g_1^2 + g_2^2)^2 - g_1^2 g_2^2 T^2 (h^2 + H^2 + 4T^2). \quad (22)$$

In our analysis we use the above thermal masses when computing the CW and the finite temperature corrections to the tree-level potential. The full thermally-corrected effective potential is thus

$$V_{\text{eff}}(h, H, T) = V_0(h, H) + V_{\text{CW}}(h, H, T) + V_{\text{CT}}(h, H) + V_{\text{T}}(h, H, T). \quad (23)$$

3. Parameter space and considered constraints

With the full expression of the scalar potential at hand, we briefly review the constraints applied in the forthcoming analysis and define the explored region of IDM the parameter space.

3.1. Considered parameter ranges

In our analysis, we scan the parameter space shown in Tab. 1. We then use the CosmoTransitions package [54] to obtain, for each point selected, the temperature-dependent phase structure of the scalar potential and to assess the nature of the corresponding phase transitions.

<i>Parameter</i>	<i>Range</i>
m_H	[10, 1000] GeV
m_A	[10, 1000] GeV
m_{H^+}	[10, 1000] GeV
λ_2	$[0, \frac{4\pi}{3}]$
λ_{345}	$[-1.47, 4\pi]$

Table 1: The parameter ranges used in our scan. We selected only configurations with $m_H < m_A$, since H is our DM candidate. The lower bound on λ_{345} is imposed by the stability of the potential [31].

The obtained points are then selected according to the bounds discussed below.

3.2. Theoretical constraints

A first requirement is the stability of the scalar potential, which guarantees that minima appear at finite field values. For the IDM, the potential is bounded from below if the following conditions are satisfied:

$$\lambda_1 > 0, \quad \lambda_3 + 2\sqrt{\lambda_1 \lambda_2} > 0, \quad \lambda_3 + \lambda_4 - |\lambda_5| + 2\sqrt{\lambda_1 \lambda_2} > 0. \quad (24)$$

A charge-breaking vacuum is avoided by $\lambda_4 - |\lambda_5| < 0$, which always holds if H^\pm is heavier than the DM candidate H [33].

Perturbative unitarity requires that the combinations of couplings e_i from the eigenvalues of the two-to-two scattering matrix be bounded: $|e_i| < 8\pi$. From the full 22×22 S -matrix [55], we have [31] $e_{1,2} = \lambda_3 \pm \lambda_4$, $e_{3,4} = \lambda_3 \pm \lambda_5$, $e_{5,6} = \lambda_3 + 2\lambda_4 \pm 3\lambda_5$, $e_{7,8} = -\lambda_1 - \lambda_2 \pm \sqrt{(\lambda_1 - \lambda_2)^2 + \lambda_4^2}$, $e_{9,10} = -3\lambda_1 - 3\lambda_2 \pm \sqrt{9(\lambda_1 - \lambda_2)^2 + (2\lambda_3 + \lambda_4)^2}$, $e_{11,12} = -\lambda_1 - \lambda_2 \pm \sqrt{(\lambda_1 - \lambda_2)^2 + \lambda_5^2}$. The strongest constraints are given by $|\lambda_2| < 4\pi/3$ and $|\lambda_{345}| < 4\pi$.

3.3. Experimental constraints

The decay widths of the Z and W bosons measured at LEP with high precision preclude decays of these particles into the new states. Therefore, we require that the masses of the inert doublet components satisfy [56]

$$m_H + m_{H^\pm} > m_W, \quad m_A + m_{H^\pm} > m_W, \quad m_H + m_A > m_Z, \quad 2m_{H^\pm} > m_Z. \quad (25)$$

LEP searches for new neutral final states further exclude a range of masses [57], thereby forcing

$$m_H > 80 \text{ GeV}, \quad m_A > 100 \text{ GeV} \quad \text{or} \quad m_A - m_H < 8 \text{ GeV}, \quad (26)$$

in addition to

$$m_{H^\pm} > 70 \text{ GeV} \quad (27)$$

due to searches for charged scalar pair production [58].

Similarly, if $m_H < m_h/2$, the Higgs boson can decay into DM with a partial width of

$$\Gamma_{h \rightarrow HH} = \frac{\lambda_{345}^2 v^2}{32\pi m_h} \sqrt{1 - \frac{4m_H^2}{m_h^2}} \quad (28)$$

which is constrained by measurements of the Higgs boson invisible width. The current values provided by the ATLAS and CMS experiments [59, 60] on the invisible branching ratio $\text{BR}_{\text{inv}} = \Gamma_{h \rightarrow HH} / (\Gamma_{h \rightarrow \text{SM}} + \Gamma_{h \rightarrow HH})$ are $\text{BR}_{\text{inv}} < 0.23 - 0.36$. In the following, we will use the conservative limit $\text{BR}_{\text{inv}} < 0.23$.

Collider analyses also provide constraints on the electroweak precision observables (EWPO), sensitive to new radiative contributions in the electroweak sector. The EWPO are usually expressed via the Peskin-Takeuchi parameters S , T and U [61, 62], determined through a joint fit of the precision observables and SM predictions. Disregarding for the moment the new determination of the W boson mass by the CDF collaboration [43] (discussed in Sec. 7), the EWPO fit within the SM alone [63] gives the results presented in Tab. 2.

Parameter	Result	Correlation
S	0.06 ± 0.10	$0.90 (T), -0.57 (U)$
T	0.11 ± 0.12	$-0.82 (U)$
U	-0.02 ± 0.09	

Table 2: Peskin-Takeuchi parameters [61, 62] as determined by the electroweak precision observables [63] prior to the new W boson mass determination by the CDF collaboration [43].

The IDM contributions to the S , T and U parameters, which add to the SM result, are given by [64]

$$T = \frac{1}{32\pi^2 \alpha v^2} [F(m_{H^\pm}^2, m_A^2) + F(m_{H^\pm}^2, m_H^2) - F(m_A^2, m_H^2)], \quad (29)$$

where $F(x, y) = \frac{x+y}{2} - \frac{xy}{x-y} \ln(x/y)$ for $x \neq y$ and $f_c(x, x) = 0$ and

$$S = \frac{4 \sin^2 \theta_W}{\alpha} \frac{g^2}{384\pi^2} \left[(\cos^2 \theta_W - \sin^2 \theta_W)^2 G(m_{H^\pm}^2, m_{H^\pm}^2, m_Z^2) + G(m_H^2, m_A^2, m_Z^2) + \ln \frac{m_A^2}{m_{H^\pm}^2} + \ln \frac{m_H^2}{m_{H^\pm}^2} \right], \quad (30)$$

$$U = \frac{4 \sin^2 \theta_W}{\alpha} \frac{g^2}{384 \pi^2} \left[-(\cos^2 \theta_W - \sin^2 \theta_W)^2 G(m_{H^\pm}^2, m_{H^\pm}^2, m_Z^2) + G(m_{H^\pm}^2, m_A^2, m_W^2) + G(m_{H^\pm}^2, m_H^2, m_W^2) - G(m_H^2, m_A^2, m_Z^2) \right], \quad (31)$$

where $G(I, J, Q) \equiv -\frac{16}{3} + \frac{5(I+J)}{Q} - \frac{2(I-J)^2}{Q^2} + \frac{3}{Q} \left[\frac{I^2+J^2}{I-J} \frac{I^2-J^2}{Q} + \frac{(I-J)^3}{3Q^2} \right] \ln \frac{I}{J} + \frac{r}{Q^3} f(t, r)$, with $t \equiv I + J - Q$ and $r \equiv Q^2 - 2Q(I + J) + (I - J)^2$ and where

$$f(t, r) \equiv \begin{cases} \sqrt{r} \ln \left| \frac{t-\sqrt{r}}{t+\sqrt{r}} \right| & \text{if } r > 0 \\ 0 & \text{if } r = 0 \\ 2\sqrt{-r} \arctan \frac{\sqrt{-r}}{t} & \text{if } r < 0. \end{cases} \quad (32)$$

Notice that new EWPO contributions vanish in the limit of degenerate masses, so these observables tend to discourage hierarchical mass spectra. For the purpose of constraining the IDM parameter space, we require that the total values of S , T and U remain within the 95% joint confidence level.

Finally, the properties of our DM candidate are constrained by the latest Planck measurements, which gives the corresponding relic density as $\Omega_c h^2 = 0.120 \pm 0.001$ [3]. In our analysis we impose the 3σ upper bound indicated by the data, although we allow for the possibility that the inert doublet yield only a subdominant DM component. For the computation of the relic abundance we rely on the `micrOMEGAs` code [65].

4. Phase transitions

In the early universe, thermal evolution of the IDM effective potential can cause cosmic PTs and generate GWs. At high temperatures thermal corrections dominate the potential and force the fields to vanishing VEVs at the origin of the field space. As the temperature lowers with the expansion of the universe, additional minima appear in the scalar potential at finite field values. At the so-called critical temperature T_c , two minima are degenerated. Then at a lower temperature, PTs may then occur via tunneling across the potential barrier [66–68] (between these two minima) sourced by the thermal effect. The rate of these processes (the bubble nucleation rate due to false vacuum decay) per unit volume and time is given by [69, 70]

$$\Gamma(T) \simeq T^4 \left(\frac{S}{2\pi T} \right)^{3/2} e^{-S/T}, \quad (33)$$

where $S \equiv S(h, H, T)$ is the 3-dimensional Euclidean action computed for an $O(3)$ -symmetric critical bubble (i.e. for the “bounce” solution of the equations of motion). The PT begins at the nucleation temperature T_n . This is defined as the temperature at which one bubble nucleates per Hubble volume per Hubble time

$$\Gamma(T_n) H_n^{-4} \sim O(1), \quad (34)$$

where $H_n \equiv H(T_n)$ is the value of the Hubble parameter at T_n . For FOPTs close to the EW scale, the condition above simply amounts to the criterion $S/T_n \simeq 140$.

The PT inverse time-duration is quantified in the parameter β [71] with

$$\frac{\beta}{H_n} = T_n \frac{d(S/T)}{dT} \Big|_{T_n}, \quad (35)$$

where the adiabatic time-temperature relation $\frac{dT}{dt} = -HT$ was used. The inverse of β/H_n can also be used to estimate the number of bubbles per Hubble volume obtained at the end of the phase transition.²

²Indeed, the number of bubbles per Hubble volume during the phase transition is $\Gamma H^{-3} \beta^{-1}$. Therefore, when the PT completes at $T = T_n$, Eq. (34) indicates that H_n/β bubbles per Hubble volume were formed [71].

The PT strength, on the other hand, is quantified in the parameter [72]

$$\alpha = \frac{\Delta V_{\text{eff}} - \frac{T}{4} \Delta \frac{\partial V_{\text{eff}}}{\partial T}}{\rho_{\text{rad}}} \Big|_{T=T_n}, \quad (36)$$

where $\Delta V_{\text{eff}} \equiv V_{\text{eff}}|_{\text{false vacuum}} - V_{\text{eff}}|_{\text{true vacuum}}$ (and similarly for $\Delta \frac{\partial V_{\text{eff}}}{\partial T}$), the thermally corrected effective potential V_{eff} is defined in Eq. (23) and the radiation energy density is $\rho_{\text{rad}} = \frac{\pi^2}{30} g_* T^4$, with g_* the effective number of relativistic degrees of freedom at the temperature T .

Finally, for first-order PTs with small latent heat, the GW production begins already at temperatures of the thermal bath close to the nucleation temperature [73]. As we will show below, the use of the nucleation temperature in our computation of the GW signal (in place of the percolation temperature) is justified by the fact that the ratio β/H_n is large almost everywhere in the considered parameter space.

4.1. Phase transition patterns

The PT patterns found in our analysis are summarised in Fig. 1, which schematically shows the sequences of transitions that connect the high-temperature minimum of the IDM potential, O , to the EW vacuum phase h . The red arrow indicates one-step PTs $O \rightarrow h$, which directly connect the two minima. The blue arrows characterise two-step PTs $O \rightarrow H \rightarrow h$, in which the EW vacuum is reached after a transient phase, H , where only the inert doublet neutral component acquires a VEV. Similarly, the yellow arrows denote two-step PT patterns $O \rightarrow Hh \rightarrow h$ going through a different transient phase, Hh , in which both h and H acquire non-vanishing thermal VEVs. In our scan we have also identified three-step PTs $O \rightarrow H \rightarrow Hh \rightarrow h$ as indicated by the green arrows.

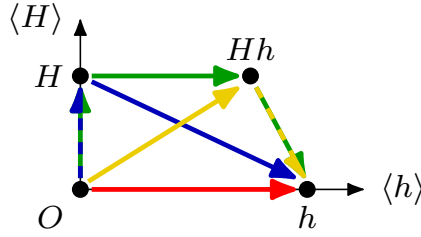


Figure 1: Schematic representation of the possible phases and PT patterns supported by the IDM scalar potential. The high-temperature minimum of the potential, where $\langle h \rangle = \langle H \rangle = 0$, is denoted with O . The phase h is characterised by $\langle h \rangle \neq 0$ and $\langle H \rangle = 0$, and includes the EW vacuum. The configuration where $\langle H \rangle \neq 0$ but $\langle h \rangle = 0$ is denoted with H , while a phase with $\langle h \rangle, \langle H \rangle \neq 0$ is indicated with Hh . The arrows show the different PT sequences identified in our analysis.

In Fig. 2 we show the regions of the IDM parameter space where the identified PTs occur. In particular, the orange region indicates that the EW vacuum is reached by using at least one FOPT, thereby sourcing a potentially detectable GW signal. Conversely, the blue region shows transitions or sequences of transitions that involve exclusively second-order phase transitions (SOPTs) in each step. In these projections of the full parameter space, the blue region is contained within the orange one.

The sequences of PTs involving at least one FOPT step are presented in isolation in Fig. 3. As we can see, most of the covered parameter space gives rise to one-step $O \rightarrow h$, whereas multi-step PTs only occur in a limited region roughly bounded by $0 \lesssim \lambda_{345} \lesssim 3$, $m_H \lesssim 250$ GeV and $m_A, m_{H^\pm} < 500$ GeV, which we scan with greater accuracy. In particular, we find that three-step PTs require $\lambda_{345} \lesssim 1.5$, while two-step PTs using a transient Hh phase are allowed only for $\lambda_{345} \lesssim 0.8$.

4.2. One-step phase transitions

Focusing on the identified one-step PTs, we show in Fig. 4 the regions of the parameter space yielding a $O \rightarrow h$ transition.

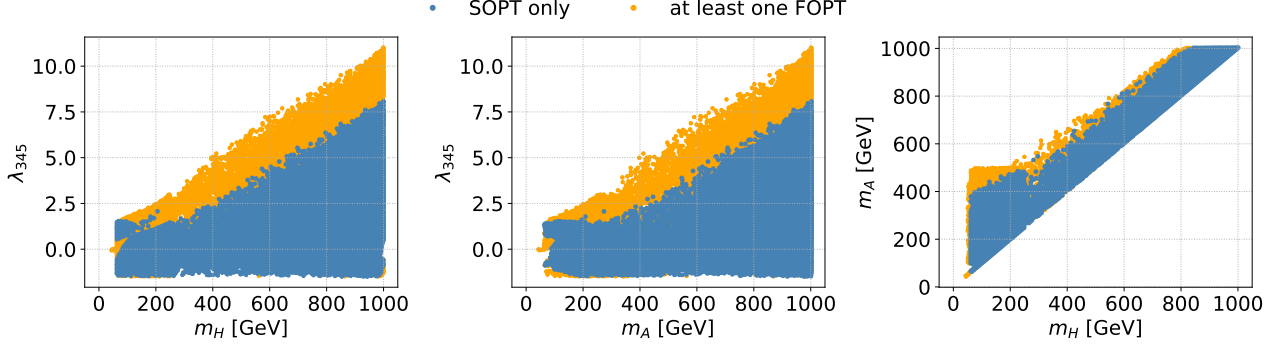


Figure 2: Projections of the IDM parameter space on the planes spanned by m_H , m_A and λ_{345} . Each panel shows the regions where the EW vacuum is achieved purely through PTs of the second order (blue) or PTs that involve at least one first-order process (orange). Points leading to DM overabundance are not shown.

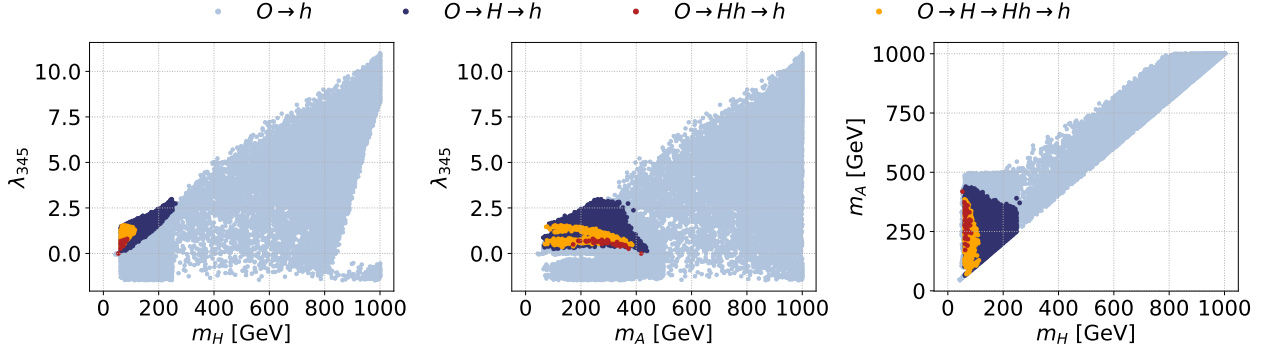


Figure 3: Projections of the IDM parameter space on the planes spanned by m_H , m_A and λ_{345} . Each panel shows the regions yielding a one-step PT $O \rightarrow h$ (light blue), a two-step PT $O \rightarrow H \rightarrow h$ (dark blue) and $O \rightarrow Hh \rightarrow h$ (red), as well as a three-step PT $O \rightarrow H \rightarrow Hh \rightarrow h$ (orange). For all these transitions, we require at least one FOPT. Points leading to DM overabundance are not shown.

The panels in the top row show the case of FOPTs, whereas SOPTs are analysed in the bottom row. In all the plots, the colour code indicates the obtained DM relic density and red stars indicate points that lead to a relic density within the experimental 3σ confidence interval.

As we can see, the considered values of scalar masses do not particularly favour either type of transition. Both FOPTs and SOPTs are furthermore uniformly distributed along the whole span of the analysed mass ranges. Comparing the plots in the first column of the figure shows that FOPTs generally require larger values of λ_{345} . For $m_H \gtrsim 800$ GeV, however, we notice that intermediate values of this coupling result exclusively in SOPTs. Close to the very end of the considered DM mass range, FOPTs thus require $\lambda_{345} \lesssim 0$ or $\lambda_{345} \gtrsim 8$. The value $\lambda_{345} \simeq 8$ also constitutes an upper bound obeyed by the SOPTs in the considered parameter space. As for the DM relic abundance, we see that FOPTs and SOPTs respectively prefer the small and large end of the investigated DM mass range. In either case, these solutions select small interval of λ_{345} values centered on $\lambda_{345} \simeq 0$.

4.3. Two-step phase transitions

We have identified two patterns of two-step PT, $O \rightarrow H \rightarrow h$ and $O \rightarrow Hh \rightarrow h$, which have a different transient phase. Such processes are particularly relevant for the phenomenological exploration of the framework, as a sequence involving two FOPTs could result in a peculiar GW signal characterised by a double peak in the frequency spectrum.

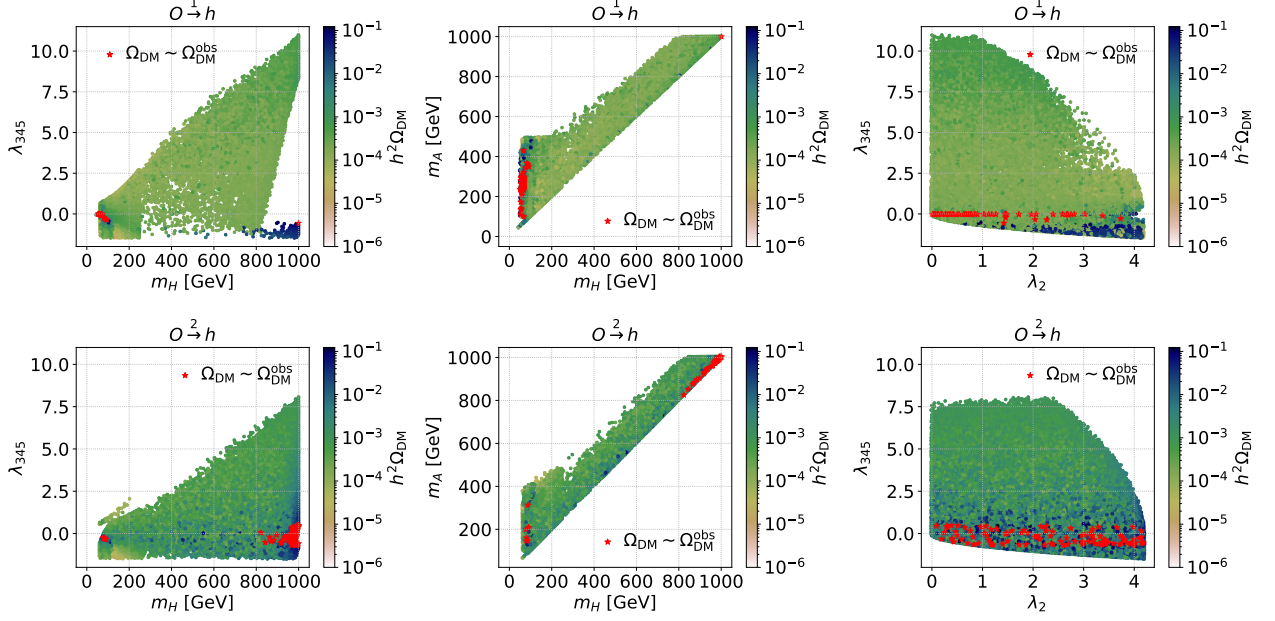


Figure 4: Regions in the IDM parameter space yielding one-step PT $O \rightarrow h$. The three panels at the top illustrate the case of first-order PTs, while the bottom three panels show second-order PTs. The colour code indicates the obtained DM abundance, which agrees with the measured 3σ range in correspondence of red stars. Points leading to DM overabundance are not shown.

Focusing for the moment on the sequence $O \rightarrow H \rightarrow h$, we notice that almost always these processes involve at least one FOPT step. The occurrence of this sequence in parameter space is shown in Fig. 5. In the left panel, the linear trend between λ_{345} and m_H correlates with the produced dark matter abundance for $m_H \lesssim 200$ GeV, but it remains below the observed 3σ range even in the favoured low energy region. The middle panel shows that the DM abundance is relatively insensitive to the value of m_A for a given DM mass and that, for large values of m_H , these solutions require a mild hierarchy between the new neutral states. The last plot, instead, shows that the obtained DM abundance is relatively insensitive to the strength of DM self-interactions regulated by λ_2 . We stress that such solutions only yield an under-abundant DM relic density.

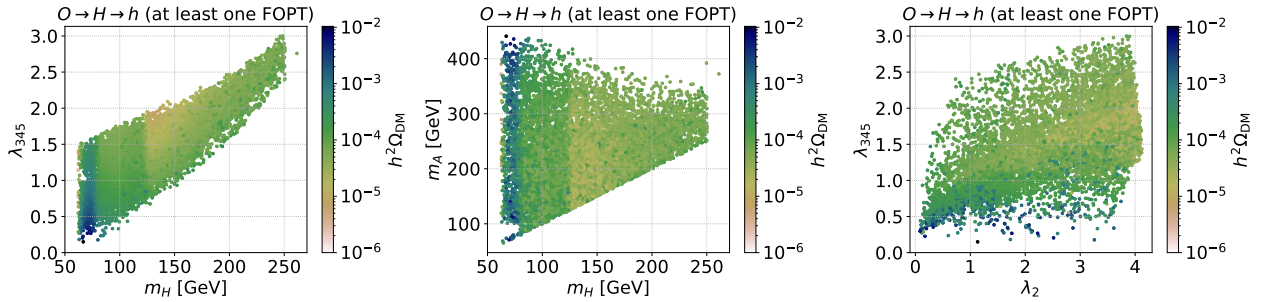


Figure 5: Regions in the IDM parameter space yielding two-step PT $O \rightarrow H \rightarrow h$ involving at least one FOPT. The colour code indicates the obtained DM abundance, which for these solutions always falls below the 3σ range found by the Planck measurements. Points leading to DM overabundance are not shown.

Similarly to the previous case, the PT pattern $O \rightarrow Hh \rightarrow h$ predominantly has at least one FOPT. The values of the IDM parameters supporting this kind of transitions are shown in Fig. 6. As we can see, these solutions are rarer than those using a transient H phase and select a narrow region in the IDM parameter space mostly characterised by small but positive values of λ_{345} and a mild mass hierarchy of the neutral scalar states.

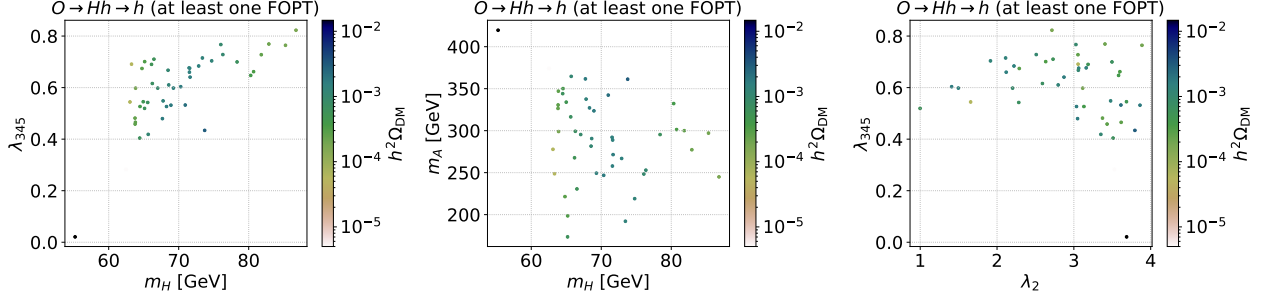


Figure 6: Regions in the IDM parameter space yielding the two-step PT $O \rightarrow Hh \rightarrow h$ involving at least one FOPT. The colour code indicates the obtained DM abundance, which for these solutions always falls below the 3σ range found by the Planck measurements. Points leading to DM overabundance are not shown.

4.4. Three-step phase transitions

Three-step PTs generally occur for DM masses in a interval roughly given by $m_h/2 \lesssim m_H \lesssim m_h$ and require moderate values of the λ_{345} coupling. Fig. 7 shows the processes of this kind that we identified in our analysis, putting in evidence the IDM parameter space where at least one FOPT is involved in the transition chain. As we can see from the plots in the first row, this kind of solutions requires a mild hierarchy in the neutral scalar sector that reduces with increasing DM mass and is fairly insensitive to the strength of DM self interaction. Processes involving exclusively SOPTs, shown in the bottom row, are more common and generally require a more compact mass spectrum as well as larger values of λ_2 . By comparing these two kinds of solutions, we see that processes with $\lambda_2 \lesssim 2.5$, $m_A \gtrsim 275$ GeV or $\lambda_{345} \lesssim 0.75$ necessarily involve at least one FOPT.

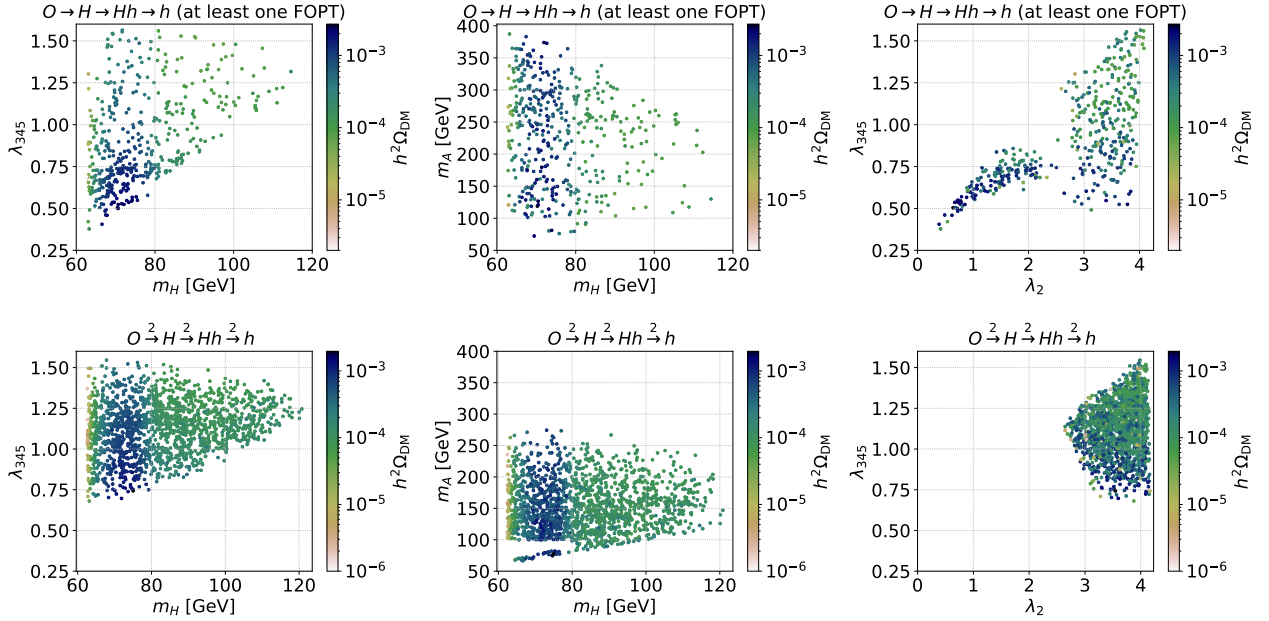


Figure 7: Regions in the IDM parameter space yielding three-step PTs $O \rightarrow H \rightarrow Hh \rightarrow h$. The top row shows transitions where at least one of the steps is of the first order. The solutions shown in the bottom row, instead, have only SOPTs. In all the plots, the colour code indicates the obtained DM relic density. Points leading to DM overabundance are not shown.

We can see that DM relic density increase near the Higgs resonance region ($m_H \sim m_h/2$), as expected. Furthermore, we point out that the white region for small m_A is due to the collider constraints, which force $m_A \gtrsim 100$ GeV or an almost degenerate neutral scalar mass spectrum. As a final remark, let us mention that we do not find three-step

PTs with three FOPT in our scan.

4.5. Phase-transition parameters

To conclude, we study correlations between the parameters that characterise the obtained PTs. Fig. 8 shows that all first-order phase transitions establish a linear relation between β/H_n and α , as expected. In fact, the shorter the FOPT is (large β/H_n), the weaker it is (small α) and vice versa. This is due to the fact that bubbles have less time to grow in a fast FOPT, and thereby store less energy in their shell before colliding. By contrast, in a slower FOPT, bubbles have significantly grown and thus accumulated energy before colliding with each other. Note that a large value of β/H_n signals that the PT dynamics proceeds much faster than the expansion of the universe and, therefore, that the latter can be safely neglected. We also observe that the strongest (and thus the shortest) FOPTs take place in the one-step $O \rightarrow h$ pattern.

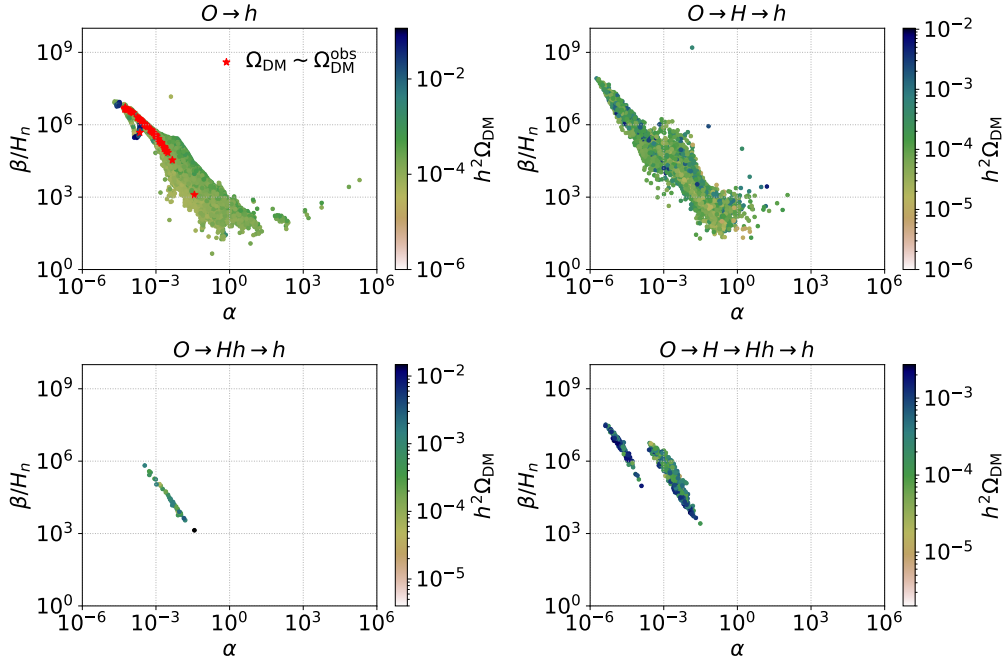


Figure 8: Correlation between the phase transition parameters α (36) and β/H_n (35) in the four phase-transition patterns identified. The colour code indicates the value of the obtained DM relic abundance, which is within the Planck 3σ range where marked with red stars. Points leading to DM overabundance are not shown.

Finally, we look for correlation in the $T_c - T_n$ space shown in Fig. 9. Most of the points yield low values of v_n/T_n , and larger values of v_n/T_n are only found for low T_c and T_n , with $v_n \equiv \sqrt{\langle H \rangle_n^2 + \langle h \rangle_n^2}$ being the VEV of the true vacuum at the nucleation temperature. Indeed, the latter generally increases when T_n decreases, and thus v_n/T_n increases as well. This behaviour can be intuitively explained as follows: for large T_n , v_n can be small and subsequently evolve smoothly toward its final value as the temperature decreases; by contrast, small T_n forces larger v_n as the system has less time left to evolve smoothly toward its tree-level value. The range of values for v_n/T_n is much smaller for multi-step phase transitions because the minimal value found for T_n is larger than in the one-step case. Furthermore, in each panel, most of the points fall close to the dashed line signalling where $T_c = T_n$. For these points, the transition takes place close to the moment where the false and true vacua become degenerated (at T_c), implying that a weak FOPT (small α) with negligible supercooling drives the process. The phase transitions become stronger ($T_c - T_n$ increases) as the temperature decreases.

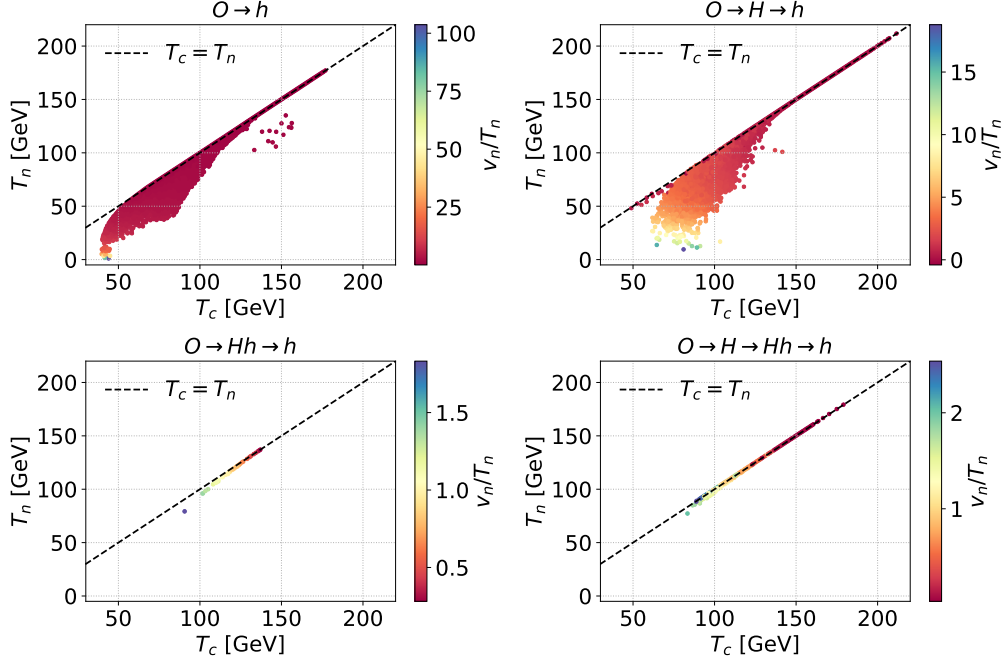


Figure 9: Correlation between the nucleation temperature, T_n , and the critical temperature, T_c , for the four phase-transition patterns identified. The colour code indicates the value of the ratio v_n/T_n , with $v_n \equiv \sqrt{\langle H \rangle_n^2 + \langle h \rangle_n^2}$ being the VEV of the true vacuum at the nucleation temperature. The dashed line indicates where the critical and nucleation temperature are equal. Points leading to DM overabundance are not shown.

5. Impact of direct detection experiments and future collider searches

Before proceeding with the analysis of the resulting GW signal, we consider a further bound given by the direct detection experiments, which probe the spin-independent cross section of DM on nuclei. To this purpose, we show in Fig. 10 the obtained spin-independent scattering cross section σ_{SI} as function of the DM mass, highlighting the different transition pattern identified. The analysis is presented separately for processes involving at least one FOPT (left panel) or exclusively SOPTs (right panel). Because we allow for DM under-abundances, the plots have been obtained by re-scaling the cross section with the fraction $\Omega_{\text{DM}}/\Omega_{\text{DM}}^{\text{Planck}}$, where Ω_{DM} is the DM abundance produced by the IDM and $\Omega_{\text{DM}}^{\text{Planck}}$ the value given by the latest Planck measurement [3]. The indicated experimental bounds use the 2018 release of the XENON1T data [5] and the 2021 PandaX-4T result [6].

As we can see, most of the multi-step PTs fall above of the considered exclusion bounds in both the cases. These processes may still occur near the Higgs resonance region ($m_H \simeq m_h/2$), where resonance effects allow for the lower values of the λ_{345} coupling required by these solutions. Another region of interest is for $m_H \in [120, 160]$ GeV, precluded for solutions involving only SOPTs and resulting in a signal borderline with the current exclusions for processes involving at least one FOPT. Contrary to the Higgs resonance region, these solutions select only multi-step PTs following the pattern $O \rightarrow H \rightarrow h$ and yield underabundant DM.

The bounds of monojet searches, that target the production of DM at colliders, are currently less stringent than the exclusions due to direct detection experiment and Higgs measurements [31, 32]. Nevertheless, the future LHC data has the potential to competitively probe the low end of the allowed DM mass range with these searches. In our analysis, we use the available projections of the monojet reach to highlight the phase transition patterns and the GW signal supported by the parameter space accessible to the high luminosity (HL) LHC run.

The results obtained are shown in Fig. 11, where again we distinguish between patterns with at least one FOPT (left panel) and those proceeding purely through SOPTs (right panel). As we can see, the HL-LHC monojet searches have the power to completely probe IDM multi-step PT, barring a small region around $m_H \simeq 130$ GeV accessible only to patterns with at least one FOPT. This region, however, will likely be probed in direct detection

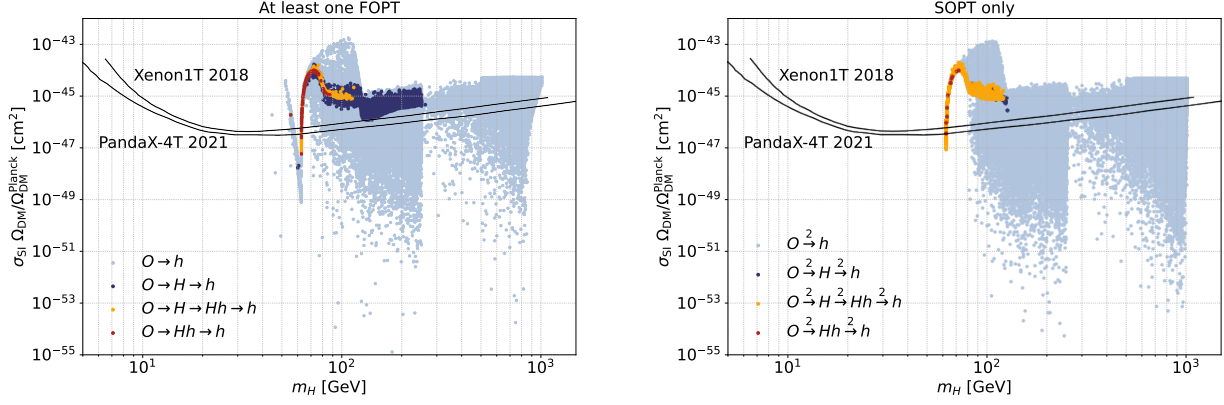


Figure 10: Spin-independent direct-detection cross section as function of the DM mass for transition patterns involving at least one FOPT (left panel) or exclusively SOPTs (right panel). The colour code highlights the pattern type: one-step PT $O \rightarrow h$ (light blue), two-step PT $O \rightarrow H \rightarrow h$ (dark blue) and $O \rightarrow Hh \rightarrow h$ (red), as well as a three-step PT $O \rightarrow H \rightarrow Hh \rightarrow h$ (orange). The experimental bounds are taken from Refs. [5, 6]. Points leading to DM overabundance are not shown.

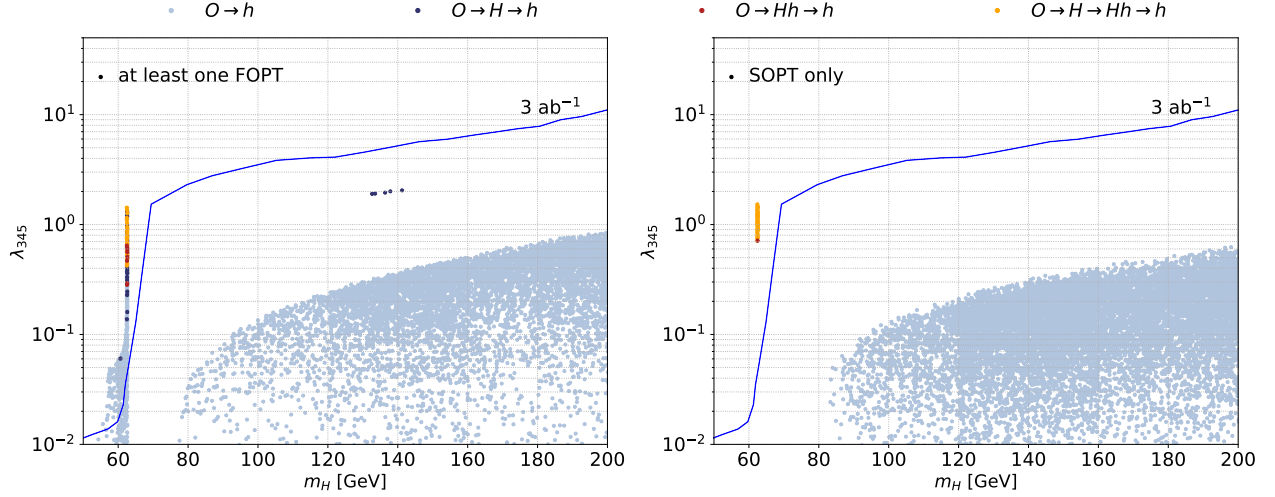


Figure 11: Power of future monojet searches [31, 32] to test IDM transition patterns involving at least one FOPT (left panel) or exclusively SOPTs (right panel). The colour code highlights the pattern type: one-step PT $O \rightarrow h$ (light blue), two-step PT $O \rightarrow H \rightarrow h$ (dark blue) and $O \rightarrow Hh \rightarrow h$ (red), as well as a three-step PT $O \rightarrow H \rightarrow Hh \rightarrow h$ (orange). Points leading to DM overabundance and excluded by Xenon1T are not shown.

experiments. Disregarding these borderline solutions, we therefore conclude that future monojet searches are crucial for establishing the viability of multi-step phase transitions within the IDM. In case of a positive detection, these experiments would also deliver a clear prediction concerning the presence of a GW counterpart to the collider signal.

6. Gravitational wave signal

6.1. Contributions to the stochastic GW background

The stochastic GW background is generated by the dynamics of the nucleated vacuum bubbles, which shape the GW power spectrum $h^2 \Omega_{\text{GW}}$ through three processes: bubble collisions, the subsequent propagation of sound

waves and through magnetohydrodynamic (MHD) turbulence. The full signal is the sum of these contributions: $h^2\Omega_{\text{GW}} \simeq h^2\Omega_{\text{col}} + h^2\Omega_{\text{sw}} + h^2\Omega_{\text{turb}}$ [73].

The emission of GW in bubble collisions can be quantified in [73]

$$h^2\Omega_{\text{col}}(f) = 1.67 \times 10^{-5} \left(\frac{H_*}{\beta} \right)^2 \left(\frac{\kappa_\phi \alpha}{1 + \alpha} \right)^2 \left(\frac{100}{g_*} \right)^{\frac{1}{3}} \left(\frac{0.11 v_w^3}{0.42 + v_w^2} \right) S_{\text{env}}(f), \quad (37)$$

where

$$S_{\text{env}}(f) = \frac{3.8 (f/f_{\text{env}})^{2.8}}{1 + 2.8 (f/f_{\text{env}})^{3.8}}, \quad (38)$$

parametrises the spectral shape of the GW radiation [74] and κ_ϕ denotes the fraction of latent heat transformed into the kinetic energy of the scalar field.

The sound wave contribution is given by [75]

$$h^2\Omega_{\text{sw}}(f) = 2.65 \times 10^{-6} \left(\frac{H_*}{\beta} \right) \left(\frac{\kappa_v \alpha}{1 + \alpha} \right)^2 \left(\frac{100}{g_*} \right)^{\frac{1}{3}} v_w S_{\text{sw}}(f), \quad (39)$$

where

$$S_{\text{sw}}(f) = (f/f_{\text{sw}})^3 \left(\frac{7}{4 + 3(f/f_{\text{sw}})^2} \right)^{7/2} \quad (40)$$

and the efficiency κ_v denotes the fraction of latent heat that is transformed into bulk motion of the fluid.

Finally, the turbulence contribution is [76, 77]

$$h^2\Omega_{\text{turb}}(f) = 3.35 \times 10^{-4} \left(\frac{H_*}{\beta} \right) \left(\frac{\kappa_{\text{turb}} \alpha}{1 + \alpha} \right)^{\frac{3}{2}} \left(\frac{100}{g_*} \right)^{1/3} v_w S_{\text{turb}}(f), \quad (41)$$

where the spectral shape is given by [76, 77]

$$S_{\text{turb}}(f) = \frac{(f/f_{\text{turb}})^3}{[1 + (f/f_{\text{turb}})]^{\frac{11}{3}} (1 + 8\pi f/h_*)} \quad (42)$$

and κ_{turb} denotes the fraction of latent heat that is transformed into MHD turbulence.

The GW signal also depends on the bubble wall velocity v_w . The determination of this parameter is very challenging and requires the microscopic calculation of the friction term and the solution of the Boltzmann equations modelling the interaction of the scalar fields driving the PT with the plasma, see for instance [78–82] for recent works. Here we consider fast moving walls, as suggested by the recent analysis [82], and we choose $v_w \simeq 1$ for simplicity.

All contributions $h^2\Omega_{\text{col}}$, $h^2\Omega_{\text{sw}}$, $h^2\Omega_{\text{turb}}$ can potentially contribute even though in our case it is the sound wave that is usually dominant.

6.2. General scan

The GW signals supported by the IDM parameter space are shown in Fig. 12, where we depict the value of the the peak of the power spectrum $h^2\Omega_{\text{GW}}^{\text{peak}}$ and the associated frequency at this peak f^{peak} for each point of scan performed.

The obtained GW signals are always dominated by the sound wave contribution. We also display the sensitivity curves of near future GW detectors LISA [15, 16], BBO [17, 18] and DECIGO [22, 23]. LISA, in particular, will probe mostly one-step transitions $O \rightarrow h$ and part of the solutions using the $O \rightarrow H \rightarrow h$ pattern. BBO and DECIGO, instead, can potentially cover most of the multi-step transition sequences we have classified. Overall, we see that single-step PTs tend to produce stronger signals. A strong signal is correlated with a large value of α , which, as shown in Fig. 8, implies a smaller value for β/H_n . Moreover, the frequency at the GW power spectrum peak is inversely proportional to the characteristic time scale of the PT, β^{-1} .³ This explains the trend in Fig. 12.

³As shown in [73], each contribution in $h^2\Omega_{\text{GW}}$ is multiplied by a factor of H_n/β (this factor is squared for bubble collisions), while in the relation for f^{peak} , a factor of β/H_n appears in each term.

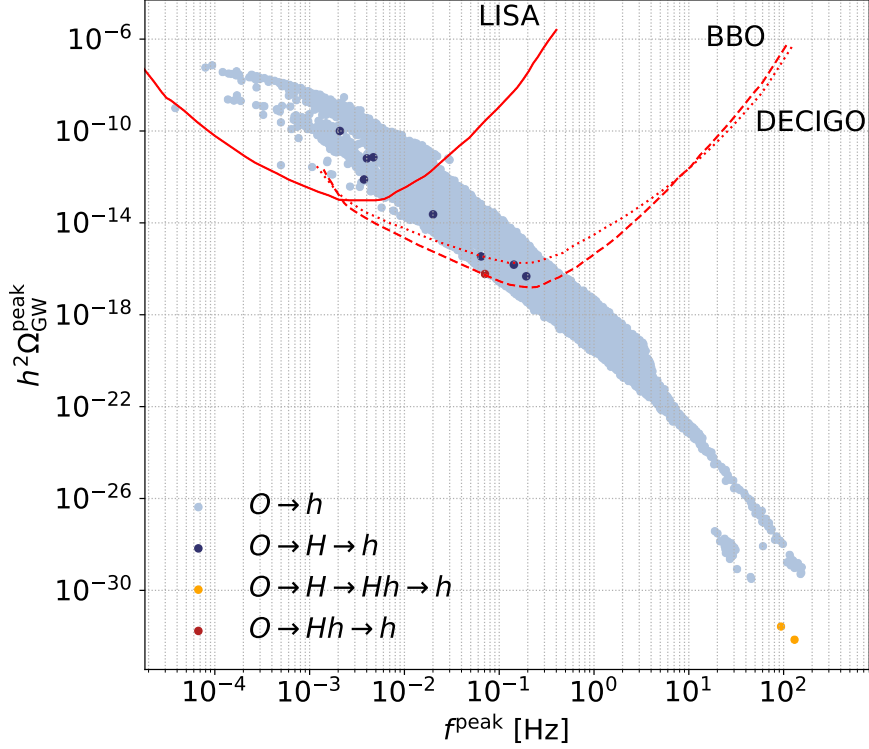


Figure 12: GW signal $h^2 \Omega_{\text{GW}}^{\text{peak}}$ as a function of the frequency f for the considered parameter space. The colour code indicates the PT pattern. Points leading to DM overabundance and excluded by Xenon1T are not shown.

While few points yielding multiple FOPTs passed our selection criteria, we note that the corresponding GW signals are generally strongly dominated by the dynamics of one of the steps. For these solutions, FOPTs initiated in the O phase are weaker than those starting from an H or Hh phase mainly because of the difference in the released vacuum energy ΔV_{eff} , which can be several orders of magnitudes larger in the latter cases. We also observe a difference in T_n , but this is usually not large enough for $\rho_{\text{rad}} \sim T^4$ to play a significant role in the discrepancies.

The analysis of the GW signal is repeated in Fig. 13, where we seek correlations with the DM relic abundance produced by the IDM focusing on one-step PT, which contribute to the bulk of the signal. As we can see, the IDM parameter space resulting in a DM relic abundance compatible with the Planck measurements, spanned mostly by solutions with $m_H \simeq m_h/2$ and $0 < \lambda_{345} \leq 0.05$, remains well below the forecast sensitivities of the analysed experiments. For these ranges of m_H and λ_{345} , we only find one-step FOPT.

In order to assess the power of the LISA experiment to probe the IDM parameter space, in Fig. 14 we have retained only one-step transitions sourcing a detectable signal. We notice the presence of two kinds of solutions: the first one selects lighter scalar masses, $m_H \lesssim 250$ GeV and $m_A \lesssim 500$ GeV, and requires limited value of the $\lambda_{345} \lesssim 2$ coupling regardless of the magnitude of λ_2 . A second class, instead, is given by larger values of the masses and of the λ_{345} parameter, but imposes an upper bound on the DM self-interactions regulated by λ_2 . As mentioned before, both of these solutions lead only to an underabundant DM relic density. The successful detection by LISA of a signal compatible with the IDM would, therefore, require the presence of other DM candidates besides the inert one.

6.3. Benchmark points

For closer study, we analyse a number of benchmark points obtained from the configuration $m_A = 400$ GeV, $m_{H^+} = 235$ GeV, $\lambda_2 = 3$ and $\lambda_{345} = 0.6$ by varying m_H . As shown in Tab. 3, the considered range of m_H scans across different PT patterns: lower masses give three-step PTs, while masses above about 70 GeV yield a single-step PT. The fraction of produced DM relic abundance progressively diminishes with increasing values of

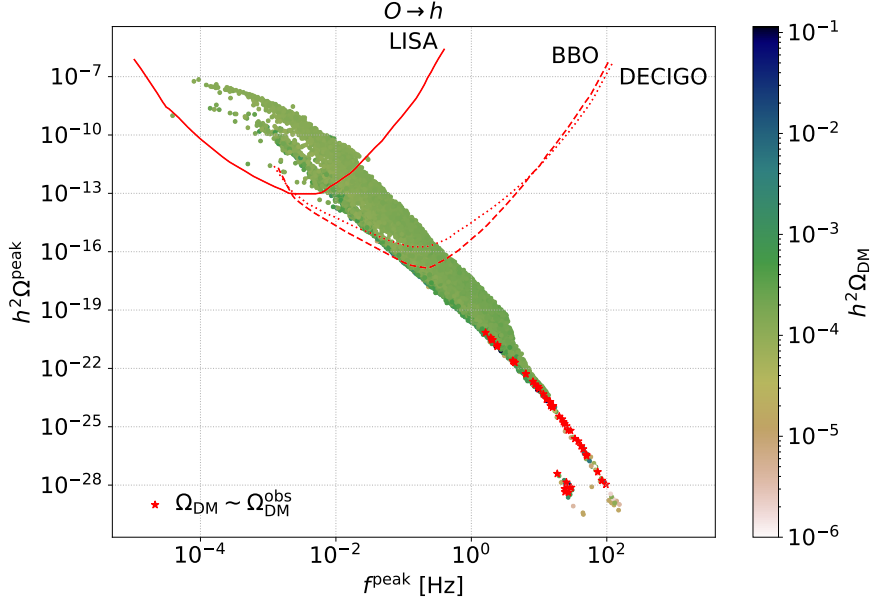


Figure 13: GW signal $h^2 \Omega_{\text{GW}}^{\text{peak}}$ as function of the frequency f for one-step FOPT $O \rightarrow h$. The colour code indicates the obtained DM relic density, which is within the Planck 3σ range for the red stars.

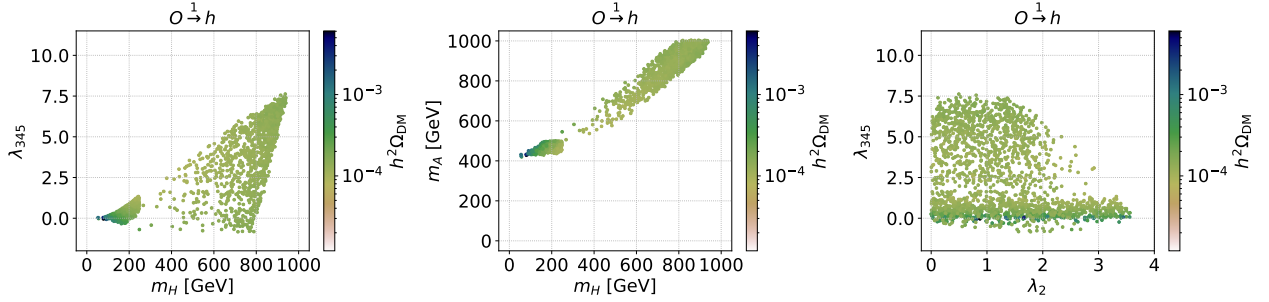


Figure 14: IDM parameter space yielding a gravitational wave signal detectable at LISA [15, 16]. The colour code indicates the produced DM abundance. Points leading to DM overabundance and excluded by Xenon1T are not shown.

m_H , stabilizing to the permille level in the high end of the considered range.

Finally, setting $m_H = 70$ GeV and the remaining parameters around the values used in Tab. 3, we checked the impact of a varying DM quartic coupling λ_2 on the strength of the GW signal. The results obtained are presented in Fig. 15, showing that an increase in the coupling usually causes a decrease in the signal. Moreover, as mentioned in Sec. 6.2, we clearly see that a FOPT from the origin O is generally weaker than the subsequent FOPT.

7. Implication of the new CDF result on the W boson mass

The CDF collaboration has recently released a new determination of the W boson mass based on the full Tevatron data, finding [43]

$$m_W^{\text{CDF}} = (80.43335 \pm 0.0094) \text{ GeV}. \quad (43)$$

The value is in strong tension with the corresponding result of global EW observable fits performed within the SM framework [83]

$$m_W^{\text{EW}} = (80.357 \pm 0.006) \text{ GeV}, \quad (44)$$

m_H (GeV)	Phase transition	T_c (GeV)	α	β/H_n	$\Omega_{\text{DM}}/\Omega_{\text{DM}}^{\text{Planck}}$
10	$O \xrightarrow{2} H \xrightarrow{1} Hh \xrightarrow{2} h$	158.62	—	—	0.106
	$O \xrightarrow{2} H \xrightarrow{1} Hh \xrightarrow{2} h$	112.59	2.82×10^{-3}	8.00×10^4	
	$O \xrightarrow{2} H \xrightarrow{1} Hh \xrightarrow{2} h$	17.09	—	—	
40	$O \xrightarrow{2} H \xrightarrow{1} Hh \xrightarrow{2} h$	148.93	—	—	0.038
	$O \xrightarrow{2} H \xrightarrow{1} Hh \xrightarrow{2} h$	113.02	3.60×10^{-3}	5.01×10^4	
	$O \xrightarrow{2} H \xrightarrow{1} Hh \xrightarrow{2} h$	73.20	—	—	
50	$O \xrightarrow{1} H \xrightarrow{1} Hh \xrightarrow{2} h$	142.70	1.06×10^{-6}	2.33×10^8	0.014
	$O \xrightarrow{1} H \xrightarrow{1} Hh \xrightarrow{2} h$	113.68	4.03×10^{-3}	4.00×10^4	
	$O \xrightarrow{1} H \xrightarrow{1} Hh \xrightarrow{2} h$	85.73	—	—	
70	$O \xrightarrow{1} H \xrightarrow{1} Hh \xrightarrow{2} h$	121.13	1.26×10^{-5}	6.37×10^6	0.004
	$O \xrightarrow{1} H \xrightarrow{1} Hh \xrightarrow{2} h$	115.45	5.43×10^{-3}	2.16×10^4	
	$O \xrightarrow{1} H \xrightarrow{1} Hh \xrightarrow{2} h$	107.36	—	—	
80	$O \xrightarrow{1} h$	116.32	6.65×10^{-3}	1.13×10^4	0.001
210	$O \xrightarrow{1} h$	138.47	3.39×10^{-4}	2.32×10^3	0.002
220	$O \xrightarrow{2} h$	139.84	—	—	0.002
230	$O \xrightarrow{2} h$	141.36	—	—	0.002

Table 3: Benchmark points: $m_A = 400$ GeV, $m_{H^\pm} = 235$ GeV, $\lambda_2 = 3$, $\lambda_{345} = 0.6$ and varying m_H . The quantity $\Omega_{\text{DM}}/\Omega_{\text{DM}}^{\text{Planck}}$ is the fraction that the IDM contributes to the observed DM relic density. For each line, the PT step in bold is the step detailed in this line.

yielding a deviation of about 7σ from the SM expectation. Importantly, the new CDF result is also departing significantly from the outcome of the analysis performed by the ATLAS collaboration on the LHC data, which finds $M_W = 80.370 \pm 0.0019$ GeV [84]. Pending new experimental inputs by the ATLAS and CMS collaboration, necessary to crosscheck the CDF claim, the anomaly seems to strongly suggest the presence of new physics contributions affecting the EW sector. In regard of this, as first pointed out in Ref. [44], the additional scalar bosons included in the IDM framework would allow to explain the new CDF result without violating the constraints imposed by the mentioned new physics searches.

Assuming this interpretation of the W mass anomaly, in the present section we reanalyse the impact that the new CDF result, if confirmed, would have on the results discussed in the previous sections. To this purpose, we repeat our scan considering the ranges of the Peskin-Takeuchi parameters shown in Tab. 4, derived through a global fit of EWPOs that accounts for the new m_W value [63].

Parameter	Result	Correlation
S	0.06 ± 0.10	$0.90 (T), -0.59 (U)$
T	0.11 ± 0.12	$-0.85 (U)$
U	0.14 ± 0.09	

Table 4: Peskin-Takeuchi parameters [61, 62] as determined by the electroweak precision observables [63] accounting for new W boson mass determination by the CDF collaboration [43].

As a first step, we verify that the IDM contribution can fully explain the W mass value proposed by the CDF collaboration. To this purpose, in Fig. 16 we show the regions of the IDM parameter space yielding a value of m_W that falls within the 1σ range of the CDF result. In order to facilitate the comparison with Fig. 3, we have

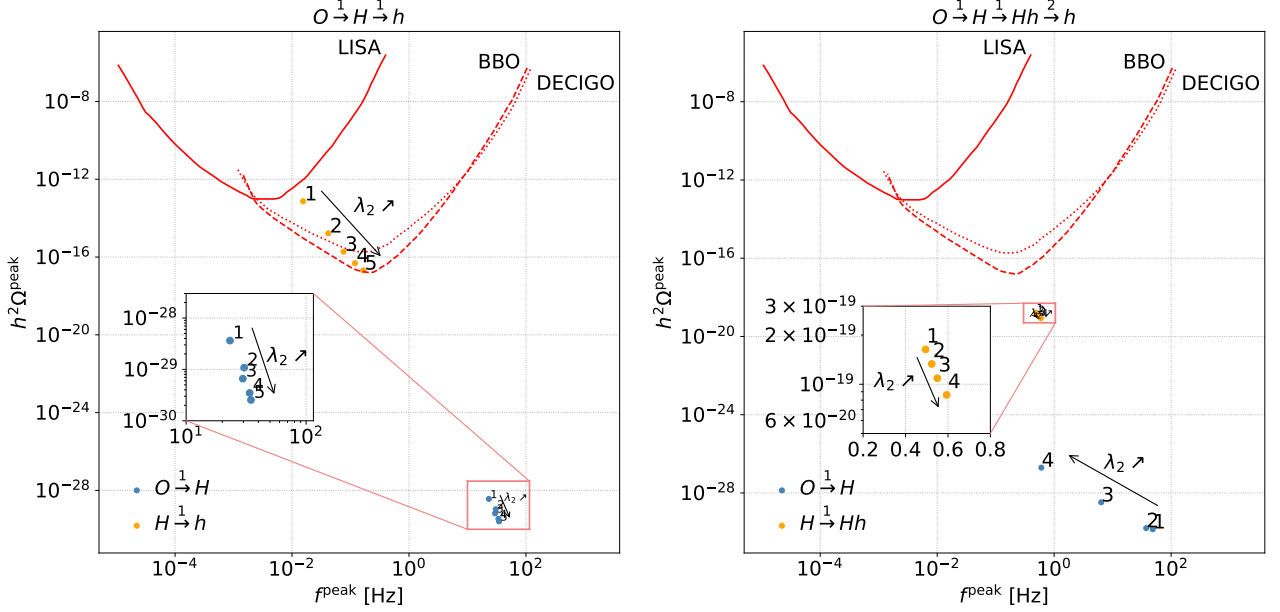


Figure 15: Left panel: Gravitational wave signal $h^2 \Omega^{\text{peak}}$ plotted as function of the frequency f for a benchmark 2-step PT with $m_H = 70$ GeV, $m_A = 400$ GeV, $m_{H^+} = 235$ GeV, $\lambda_{345} = 0.6$ and $\lambda_2 \in [0.7, 1.1]$. Right panel: The same signal for a benchmark 3-step PT with $m_H = 68$ GeV, $m_A = 398$ GeV, $m_{H^+} = 233$ GeV, $\lambda_{345} = 0.6$ and $\lambda_2 \in [2.9, 3.2]$.

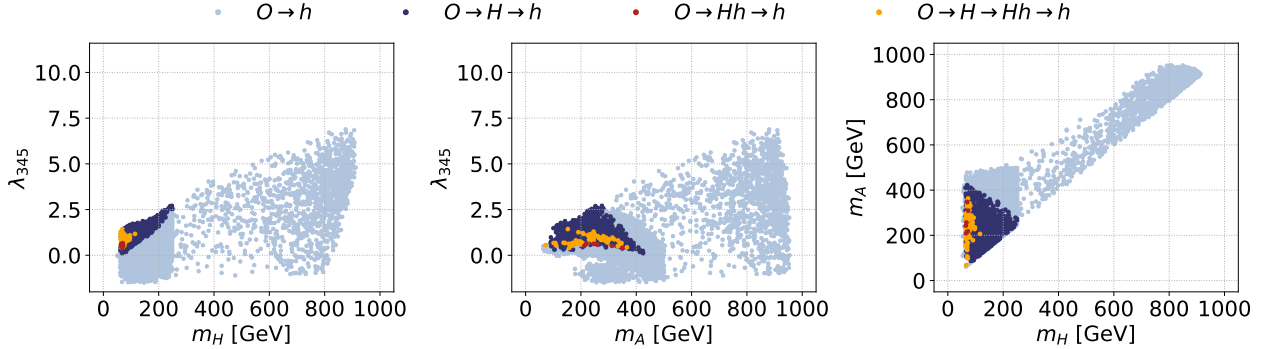


Figure 16: IDM parameter space selected by the CDF result on the W boson mass. All the points yield a value of m_W within the 1σ range indicated by the collaboration [43]: $m_W^{\text{CDF}} = (80.43335 \pm 0.0094)$ GeV. The colour code denotes the PT pattern: one-step PTs $O \rightarrow h$ (light blue), two-step PTs $O \rightarrow H \rightarrow h$ (dark blue) and $O \rightarrow Hh \rightarrow h$ (red), as well as three-step PTs $O \rightarrow H \rightarrow Hh \rightarrow h$ (orange). All the transitions involve at least one FOPT. Points leading to DM overabundance are not shown.

showed again only patterns that involve at least one first-order transition. As we can see, the new determination of m_W does not preclude any of the transition patterns identified before and the distribution of the solution remains qualitatively the same. We notice the presence of an upper bound $\lambda_{345} \lesssim 7$, not observed in the previous analysis, and the lack of solutions characterised by negative values of λ_{345} and $m_H \gtrsim 800$ GeV.

We continue the analysis in Fig. 17, where we re-analyze the results obtained for the DM spin-independent cross section on nuclei probed in direct detection experiment. As we can see, assuming the CDF determination of the W boson mass strongly reduces the number of solutions that comply with the direct detection bounds for $m_H \gtrsim 100$ GeV. The effect is particularly evident for patterns with at least one FOPT (left panel), where the bulk of one-step transitions is now excluded and multi-step transitions are only allowed in the region of DM mass close to $m_h/2$.

The reduction of viable solutions is also appreciable for patterns with SOPTs only (right panel), although it is less stringent. In this case, a sizeable number of one-step transitions remains well below the exclusion bounds of direct detection experiments, but multi-step transitions are essentially excluded.

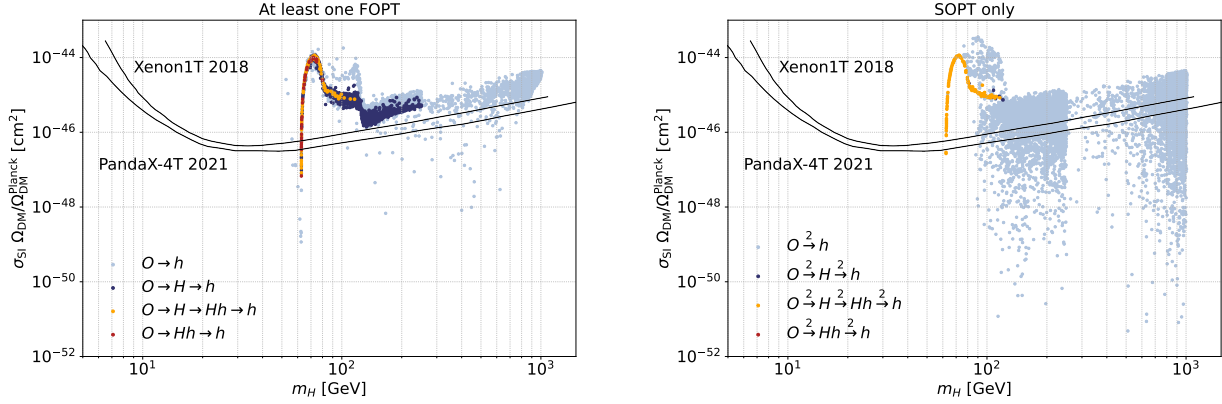


Figure 17: Spin-independent direct-detection cross section as function of the DM mass for transition patterns involving at least one FOPT (left panel) or exclusively SOPTs (right panel). This plot assumes the new CDF W -mass result. The colour code highlights the pattern type: one-step PT $O \rightarrow h$ (light blue), two-step PT $O \rightarrow H \rightarrow h$ (dark blue) and $O \rightarrow Hh \rightarrow h$ (red), as well as a three-step PT $O \rightarrow H \rightarrow Hh \rightarrow h$ (orange). The experimental bounds are taken from Refs. [5, 6]. Points leading to DM overabundance are not shown.

Retaining only the points allowed by the direct detection bounds and computing the implied GW signals, we find that the CDF value of m_W yields no qualitative difference with respect to the results presented in Sec. 6. The GW spectrum is still dominated by the contribution of one-step PTs and the dependence of the signal on the peak frequency is essentially left unmodified. One minor difference pertains to the parameter space yielding a signal within the range of the LISA experiment, where we have noticed the presence of a sharper upper bound $\lambda_{345} \lesssim 6$ affecting the second class of solutions previously discussed at the end of Sec. 6.2.

8. Conclusions

The inert doublet model is a simple extension of the Standard Model that yields a wide range of phenomenological consequences spanning from collider physics to cosmology. This framework, in particular, offers a natural dark matter candidate and predicts the appearance of additional scalar degrees of freedom at mass scales typically not much larger than the electroweak scale. Although the dark matter phenomenology and collider constraints of this model have been thoroughly studied, the cosmic phase transitions supported by its scalar potential, as well as the implied gravitational wave signals, have not been paid enough attention to. With the present paper we intended to address this issue with a comprehensive exploration of the phase structure and possible transitions supported by the inert doublet model. In our work we took into account available collider constraints, electroweak precision observables and theoretical bounds imposed by stability of the potential and perturbativity. Furthermore, the latest results of dark matter experiments have been used to investigate the properties of the neutral scalar component of the inert doublet, assumed to provide at least a subdominant dark matter component.

Our study of the thermal evolution of the scalar potential has given a full characterization of the possible phase transition patterns supported by the inert doublet model (see Fig. 1). Although in most of the parameter space the electroweak vacuum is reached through a single phase transition, our analysis shows well-defined parameter regions where the electroweak vacuum is reached via a chain of consecutive phase transitions. Both two-step and three-step phase transitions with different transient phases (where only the inert doublet or both the doublets acquire a vacuum expectation value) are possible. In Fig. 2 we detail the parameter space required to have first-order phase transitions potentially detectable through gravitational wave signal. For example, a negative or large value of the λ_{345} quartic coupling is required to have a single-step first-order phase transition. Multi-step transitions can occur when the inert doublet components are not heavier than a few hundred GeV and couplings have moderate values,

as shown in Fig. 3 for patterns involving at least one first-order step. After studying each of the identified transition chains separately, we show in Tab. 3, for a benchmark point, how the dark matter mass affects the pattern and strength of the phase transitions. Fig. 15 shows instead the dependence on dark matter self-interactions regulated by λ_2 .

By cross-correlating the identified phase transition patterns with dark matter phenomenology, we find that the inert doublet model can explain the observed relic abundance only in a part of its parameter space where the electroweak vacuum is reached through single-step processes of either order. Although multi-step phase transition patterns are associated with a significant dark matter underdensity, we see that dark matter direct detection experiments are able to tightly constrain these solutions. Focusing on patterns that involve at least one first-order phase transition, Fig. 10 shows that the direct detection bounds allow for multi-step phase transitions almost exclusively for dark matter masses close to half the Higgs boson mass. Importantly, as shown in Fig. 11, these solutions can be fully tested with the upcoming high-luminosity LHC monojet searches.

After applying the results of direct detection searches as a further constraint, we have investigated the gravitational wave spectra produced by different phase transition patterns. The results, gathered in Fig. 12, show that one-step processes dominate the signal. Future gravitational wave experiments will probe a part of these solutions yielding a significant dark matter underdensity, implying that the detection of a compatible signal would require another dark matter component. Focusing on the reach of the LISA experiment, we have shown in Fig. 14 the part of the inert doublet model parameter space which LISA is able to constrain. Whereas few points with multiple first-order phase transitions fall above the sensitivity curves of the considered experiments, we find that the generated gravitational signal is always strongly dominated by the transitions initiated during the transient phase at intermediate temperature. Therefore, it is highly unlikely that such transitions will induce a gravitational wave signal with two separate distinguishable peaks at different frequencies.

Finally, we have investigated the impact of the recent re-determination of the W boson mass presented by the CDF collaboration on our conclusions, under the assumption that the inert doublet model be responsible for the observed anomaly. After performing a dedicated scan that accounts for the shift of the Peskin-Takeuchi parameters implied by the new CDF result, in Sec. 7 we have repeated the analysis concerning phase transition patterns and corresponding gravitational wave signals. Whereas all the patterns previously identified remain viable, we find that the number of solution complying with the direct detection bound for dark matter masses above 100 GeV is strongly reduced. For transition chains with at least one first-order step, adopting the CDF determination of m_W forces the bulk of acceptable solutions to fall in the Higgs resonance region, where the λ_{345} coupling that regulates also the direct detection cross section is smaller. A similar reduction is observable also for patterns that proceed solely through second-order phase transitions, albeit with reduced intensity. In this case, however, single-step solutions are strongly favoured. We have found no significant difference between the gravitational wave signals implied by this dataset and the results previously obtained by disregarding the anomaly.

Acknowledgements

This work was supported by the Estonian Research Council grants PRG434 and PRG356, by the European Regional Development Fund and the programme Mobilitas Plus grants MOBTT5 and MOBTT86, and by the EU through the European Regional Development Fund CoE program TK133 “The Dark Side of the Universe”. The work of LDR has been partially supported by a fellowship from “la Caixa” Foundation (ID 100010434) and from the European Union’s Horizon 2020 research and innovation programme under the Marie Skłodowska-Curie Action grant agreement No 847648.

References

- [1] CMS collaboration, *Observation of a New Boson at a Mass of 125 GeV with the CMS Experiment at the LHC*, *Phys. Lett. B* **716** (2012) 30 [[1207.7235](#)].
- [2] ATLAS collaboration, *Observation of a new particle in the search for the Standard Model Higgs boson with the ATLAS detector at the LHC*, *Phys. Lett. B* **716** (2012) 1 [[1207.7214](#)].

- [3] Planck collaboration, *Planck 2018 results. VI. Cosmological parameters*, *Astron. Astrophys.* **641** (2020) A6 [[1807.06209](#)].
- [4] LUX collaboration, *Results from a search for dark matter in the complete LUX exposure*, *Phys. Rev. Lett.* **118** (2017) 021303 [[1608.07648](#)].
- [5] XENON collaboration, *Dark Matter Search Results from a One Ton-Year Exposure of XENON1T*, *Phys. Rev. Lett.* **121** (2018) 111302 [[1805.12562](#)].
- [6] PandaX-4T collaboration, *Dark Matter Search Results from the PandaX-4T Commissioning Run*, *Phys. Rev. Lett.* **127** (2021) 261802 [[2107.13438](#)].
- [7] ATLAS collaboration, *Constraining the Dark Sector with the monojet signature in the ATLAS experiment*, .
- [8] LIGO Scientific, Virgo collaboration, *Observation of Gravitational Waves from a Binary Black Hole Merger*, *Phys. Rev. Lett.* **116** (2016) 061102 [[1602.03837](#)].
- [9] LIGO Scientific, Virgo collaboration, *GW151226: Observation of Gravitational Waves from a 22-Solar-Mass Binary Black Hole Coalescence*, *Phys. Rev. Lett.* **116** (2016) 241103 [[1606.04855](#)].
- [10] K. Kajantie, M. Laine, K. Rummukainen and M.E. Shaposhnikov, *Is there a hot electroweak phase transition at $m_H \gtrsim m_W$?*, *Phys. Rev. Lett.* **77** (1996) 2887 [[hep-ph/9605288](#)].
- [11] Y. Aoki, F. Csikor, Z. Fodor and A. Ukawa, *The Endpoint of the first order phase transition of the SU(2) gauge Higgs model on a four-dimensional isotropic lattice*, *Phys. Rev. D* **60** (1999) 013001 [[hep-lat/9901021](#)].
- [12] C.J. Hogan, *NUCLEATION OF COSMOLOGICAL PHASE TRANSITIONS*, *Phys. Lett. B* **133** (1983) 172.
- [13] P.J. Steinhardt, *Relativistic Detonation Waves and Bubble Growth in False Vacuum Decay*, *Phys. Rev. D* **25** (1982) 2074.
- [14] E. Witten, *Cosmic Separation of Phases*, *Phys. Rev. D* **30** (1984) 272.
- [15] eLISA collaboration, *The Gravitational Universe*, [1305.5720](#).
- [16] P. Amaro-Seoane, H. Audley, S. Babak, J. Baker, E. Barausse, P. Bender et al., *Laser Interferometer Space Antenna*, *arXiv e-prints* (2017) arXiv:1702.00786 [[1702.00786](#)].
- [17] V. Corbin and N.J. Cornish, *Detecting the cosmic gravitational wave background with the big bang observer*, *Class. Quant. Grav.* **23** (2006) 2435 [[gr-qc/0512039](#)].
- [18] J. Crowder and N.J. Cornish, *Beyond LISA: Exploring future gravitational wave missions*, *Phys. Rev. D* **72** (2005) 083005 [[gr-qc/0506015](#)].
- [19] W.-R. Hu and Y.-L. Wu, *The Taiji Program in Space for gravitational wave physics and the nature of gravity*, *Natl. Sci. Rev.* **4** (2017) 685.
- [20] W.-H. Ruan, Z.-K. Guo, R.-G. Cai and Y.-Z. Zhang, *Taiji program: Gravitational-wave sources*, *Int. J. Mod. Phys. A* **35** (2020) 2050075 [[1807.09495](#)].
- [21] TianQin collaboration, *TianQin: a space-borne gravitational wave detector*, *Class. Quant. Grav.* **33** (2016) 035010 [[1512.02076](#)].
- [22] N. Seto, S. Kawamura and T. Nakamura, *Possibility of direct measurement of the acceleration of the universe using 0.1-Hz band laser interferometer gravitational wave antenna in space*, *Phys. Rev. Lett.* **87** (2001) 221103 [[astro-ph/0108011](#)].
- [23] S. Kawamura et al., *Current status of space gravitational wave antenna DECIGO and B-DECIGO*, *PTEP* **2021** (2021) 05A105 [[2006.13545](#)].
- [24] N.G. Deshpande and E. Ma, *Pattern of Symmetry Breaking with Two Higgs Doublets*, *Phys. Rev. D* **18** (1978) 2574.

- [25] E. Ma, *Verifiable radiative seesaw mechanism of neutrino mass and dark matter*, *Phys. Rev. D* **73** (2006) 077301 [[hep-ph/0601225](#)].
- [26] R. Barbieri, L.J. Hall and V.S. Rychkov, *Improved naturalness with a heavy Higgs: An Alternative road to LHC physics*, *Phys. Rev. D* **74** (2006) 015007 [[hep-ph/0603188](#)].
- [27] L. Lopez Honorez, E. Nezri, J.F. Oliver and M.H.G. Tytgat, *The Inert Doublet Model: An Archetype for Dark Matter*, *JCAP* **02** (2007) 028 [[hep-ph/0612275](#)].
- [28] A. Goudelis, B. Herrmann and O. Stål, *Dark matter in the Inert Doublet Model after the discovery of a Higgs-like boson at the LHC*, *JHEP* **09** (2013) 106 [[1303.3010](#)].
- [29] N. Blinov, J. Kozaczuk, D.E. Morrissey and A. de la Puente, *Compressing the Inert Doublet Model*, *Phys. Rev. D* **93** (2016) 035020 [[1510.08069](#)].
- [30] M.A. Díaz, B. Koch and S. Urrutia-Quiroga, *Constraints to Dark Matter from Inert Higgs Doublet Model*, *Adv. High Energy Phys.* **2016** (2016) 8278375 [[1511.04429](#)].
- [31] A. Belyaev, G. Cacciapaglia, I.P. Ivanov, F. Rojas-Abatte and M. Thomas, *Anatomy of the Inert Two Higgs Doublet Model in the light of the LHC and non-LHC Dark Matter Searches*, *Phys. Rev. D* **97** (2018) 035011 [[1612.00511](#)].
- [32] A. Belyaev, T.R. Fernandez Perez Tomei, P.G. Mercadante, C.S. Moon, S. Moretti, S.F. Novaes et al., *Advancing LHC probes of dark matter from the inert two-Higgs-doublet model with the monojet signal*, *Phys. Rev. D* **99** (2019) 015011 [[1809.00933](#)].
- [33] I.F. Ginzburg, K.A. Kanishev, M. Krawczyk and D. Sokolowska, *Evolution of Universe to the present inert phase*, *Phys. Rev. D* **82** (2010) 123533 [[1009.4593](#)].
- [34] D. Borah and J.M. Cline, *Inert Doublet Dark Matter with Strong Electroweak Phase Transition*, *Phys. Rev. D* **86** (2012) 055001 [[1204.4722](#)].
- [35] G. Gil, P. Chankowski and M. Krawczyk, *Inert Dark Matter and Strong Electroweak Phase Transition*, *Phys. Lett. B* **717** (2012) 396 [[1207.0084](#)].
- [36] N. Blinov, S. Profumo and T. Stefaniak, *The Electroweak Phase Transition in the Inert Doublet Model*, *JCAP* **07** (2015) 028 [[1504.05949](#)].
- [37] S. Fabian, F. Goertz and Y. Jiang, *Dark matter and nature of electroweak phase transition with an inert doublet*, *JCAP* **09** (2021) 011 [[2012.12847](#)].
- [38] A.P. Morais and R. Pasechnik, *Probing multi-step electroweak phase transition with multi-peaked primordial gravitational waves spectra*, *JCAP* **04** (2020) 036 [[1910.00717](#)].
- [39] D. Land and E.D. Carlson, *Two stage phase transition in two Higgs models*, *Phys. Lett. B* **292** (1992) 107 [[hep-ph/9208227](#)].
- [40] V. Zarikas, *The Phase transition of the two Higgs extension of the standard model*, *Phys. Lett. B* **384** (1996) 180 [[hep-ph/9509338](#)].
- [41] M. Aoki, T. Komatsu and H. Shibuya, *Possibility of multi-step electroweak phase transition in the two Higgs doublet models*, *2106.03439*.
- [42] J.M. Cline and K. Kainulainen, *Improved Electroweak Phase Transition with Subdominant Inert Doublet Dark Matter*, *Phys. Rev. D* **87** (2013) 071701 [[1302.2614](#)].
- [43] CDF collaboration, *High-precision measurement of the W boson mass with the CDF II detector*, *Science* **376** (2022) 170.
- [44] Y.-Z. Fan, T.-P. Tang, Y.-L.S. Tsai and L. Wu, *Inert Higgs Dark Matter for New CDF W-boson Mass and Detection Prospects*, *2204.03693*.
- [45] S.R. Coleman and E.J. Weinberg, *Radiative Corrections as the Origin of Spontaneous Symmetry Breaking*, *Phys. Rev. D* **7** (1973) 1888.

- [46] C. Delaunay, C. Grojean and J.D. Wells, *Dynamics of Non-renormalizable Electroweak Symmetry Breaking*, *JHEP* **04** (2008) 029 [[0711.2511](#)].
- [47] J.M. Cline and P.-A. Lemieux, *Electroweak phase transition in two Higgs doublet models*, *Phys. Rev. D* **55** (1997) 3873 [[hep-ph/9609240](#)].
- [48] J.M. Cline, K. Kainulainen and M. Trott, *Electroweak Baryogenesis in Two Higgs Doublet Models and B meson anomalies*, *JHEP* **11** (2011) 089 [[1107.3559](#)].
- [49] L. Dolan and R. Jackiw, *Symmetry behavior at finite temperature*, *Phys. Rev. D* **9** (1974) 3320.
- [50] G.W. Anderson and L.J. Hall, *Electroweak phase transition and baryogenesis*, *Phys. Rev. D* **45** (1992) 2685.
- [51] D.J. Gross, R.D. Pisarski and L.G. Yaffe, *Qcd and instantons at finite temperature*, *Rev. Mod. Phys.* **53** (1981) 43.
- [52] R.R. Parwani, *Resummation in a hot scalar field theory*, *Phys. Rev. D* **45** (1992) 4695.
- [53] J. Bernon, L. Bian and Y. Jiang, *A new insight into the phase transition in the early Universe with two Higgs doublets*, *JHEP* **05** (2018) 151 [[1712.08430](#)].
- [54] C.L. Wainwright, *CosmoTransitions: Computing Cosmological Phase Transition Temperatures and Bubble Profiles with Multiple Fields*, *Comput. Phys. Commun.* **183** (2012) 2006 [[1109.4189](#)].
- [55] A. Arhrib, R. Benbrik and N. Gaur, *$H \rightarrow \gamma\gamma$ in Inert Higgs Doublet Model*, *Phys. Rev. D* **85** (2012) 095021 [[1201.2644](#)].
- [56] Q.-H. Cao, E. Ma and G. Rajasekaran, *Observing the Dark Scalar Doublet and its Impact on the Standard-Model Higgs Boson at Colliders*, *Phys. Rev. D* **76** (2007) 095011 [[0708.2939](#)].
- [57] E. Lundstrom, M. Gustafsson and J. Edsjo, *The Inert Doublet Model and LEP II Limits*, *Phys. Rev. D* **79** (2009) 035013 [[0810.3924](#)].
- [58] A. Pierce and J. Thaler, *Natural Dark Matter from an Unnatural Higgs Boson and New Colored Particles at the TeV Scale*, *JHEP* **08** (2007) 026 [[hep-ph/0703056](#)].
- [59] ATLAS collaboration, *Combined measurements of Higgs boson production and decay using up to 80 fb^{-1} of proton–proton collision data at $\sqrt{s} = 13\text{ TeV}$ collected with the ATLAS experiment*, .
- [60] CMS collaboration, *Searches for invisible decays of the Higgs boson in pp collisions at $\sqrt{s} = 7, 8$, and 13 TeV* , *JHEP* **02** (2017) 135 [[1610.09218](#)].
- [61] M.E. Peskin and T. Takeuchi, *A New constraint on a strongly interacting Higgs sector*, *Phys. Rev. Lett.* **65** (1990) 964.
- [62] M.E. Peskin and T. Takeuchi, *Estimation of oblique electroweak corrections*, *Phys. Rev. D* **46** (1992) 381.
- [63] C.-T. Lu, L. Wu, Y. Wu and B. Zhu, *Electroweak Precision Fit and New Physics in light of W Boson Mass*, *2204.03796*.
- [64] W. Grimus, L. Lavoura, O.M. Ogreid and P. Osland, *The Oblique parameters in multi-Higgs-doublet models*, *Nucl. Phys. B* **801** (2008) 81 [[0802.4353](#)].
- [65] G. Belanger, A. Mjallal and A. Pukhov, *Recasting direct detection limits within micrOMEGAs and implication for non-standard Dark Matter scenarios*, *Eur. Phys. J. C* **81** (2021) 239 [[2003.08621](#)].
- [66] J. Ellis, M. Lewicki and J.M. No, *On the Maximal Strength of a First-Order Electroweak Phase Transition and its Gravitational Wave Signal*, *JCAP* **04** (2019) 003 [[1809.08242](#)].
- [67] K. Fujikura, Y. Nakai and M. Yamada, *A more attractive scheme for radion stabilization and supercooled phase transition*, *JHEP* **02** (2020) 111 [[1910.07546](#)].
- [68] D. Croon, O. Gould, P. Schicho, T.V.I. Tenkanen and G. White, *Theoretical uncertainties for cosmological first-order phase transitions*, *JHEP* **04** (2021) 055 [[2009.10080](#)].

- [69] A.D. Linde, *Fate of the False Vacuum at Finite Temperature: Theory and Applications*, *Phys. Lett. B* **100** (1981) 37.
- [70] A.D. Linde, *Decay of the False Vacuum at Finite Temperature*, *Nucl. Phys. B* **216** (1983) 421.
- [71] C. Grojean and G. Servant, *Gravitational Waves from Phase Transitions at the Electroweak Scale and Beyond*, *Phys. Rev. D* **75** (2007) 043507 [[hep-ph/0607107](#)].
- [72] J.R. Espinosa, T. Konstandin, J.M. No and G. Servant, *Energy Budget of Cosmological First-order Phase Transitions*, *JCAP* **06** (2010) 028 [[1004.4187](#)].
- [73] C. Caprini et al., *Science with the space-based interferometer eLISA. II: Gravitational waves from cosmological phase transitions*, *JCAP* **04** (2016) 001 [[1512.06239](#)].
- [74] S.J. Huber and T. Konstandin, *Gravitational Wave Production by Collisions: More Bubbles*, *JCAP* **09** (2008) 022 [[0806.1828](#)].
- [75] M. Hindmarsh, S.J. Huber, K. Rummukainen and D.J. Weir, *Numerical simulations of acoustically generated gravitational waves at a first order phase transition*, *Phys. Rev. D* **92** (2015) 123009 [[1504.03291](#)].
- [76] C. Caprini, R. Durrer and G. Servant, *The stochastic gravitational wave background from turbulence and magnetic fields generated by a first-order phase transition*, *JCAP* **12** (2009) 024 [[0909.0622](#)].
- [77] P. Binetruy, A. Bohe, C. Caprini and J.-F. Dufaux, *Cosmological Backgrounds of Gravitational Waves and eLISA/NGO: Phase Transitions, Cosmic Strings and Other Sources*, *JCAP* **06** (2012) 027 [[1201.0983](#)].
- [78] B. Laurent and J.M. Cline, *Fluid equations for fast-moving electroweak bubble walls*, *Phys. Rev. D* **102** (2020) 063516 [[2007.10935](#)].
- [79] G.C. Dorsch, S.J. Huber and T. Konstandin, *On the wall velocity dependence of electroweak baryogenesis*, *JCAP* **08** (2021) 020 [[2106.06547](#)].
- [80] G.C. Dorsch, S.J. Huber and T. Konstandin, *A sonic boom in bubble wall friction*, *JCAP* **04** (2022) 010 [[2112.12548](#)].
- [81] S. De Curtis, L.D. Rose, A. Guiggiani, A.G. Muyor and G. Panico, *Bubble wall dynamics at the electroweak phase transition*, *JHEP* **03** (2022) 163 [[2201.08220](#)].
- [82] B. Laurent and J.M. Cline, *First principles determination of bubble wall velocity*, [2204.13120](#).
- [83] Particle Data Group collaboration, *Review of Particle Physics*, *Chin. Phys. C* **40** (2016) 100001.
- [84] ATLAS collaboration, *Measurement of the W-boson mass in pp collisions at $\sqrt{s} = 7$ TeV with the ATLAS detector*, *Eur. Phys. J. C* **78** (2018) 110 [[1701.07240](#)].